The 2020 COVID-19 pandemic and atmospheric composition: back to the future

Joshua L. Laughner[1,1,1], Jessica L. Neu[2,2,2], David Schimel[2,2,2], Paul O. Wennberg[3,3,3], Kelley Barsanti[4,4,4], Kevin Bowman[2,2,2], Abhishek Chatterjee[5,5,5], Bart Croes[6,6,6], Helen Fitzmaurice[7,7,7], Daven Henze[8,8,8], Jinsol Kim[7,7,7], Eric A. Kort[9,9,9], Zhu Liu[10,10,10], Kazuyuki Miyazaki[11,11,11], Alexander J. Turner[12,12,12], Susan Anenberg[13,13,13], Jeremy Avise[14,14,14], Hansen Cao[15,15,15], David Crisp[2,2,2], Joost de Gouw[16,16,16], Annmarie Eldering[2,2,2], John C. Fyfe[17,17,17], Daniel L. Goldberg[13,13,13], Kevin R. Gurney[18,18,18], Sina Hasheminassab[19,19,19], Francesca Hopkins[20,20,20], Cesunica E. Ivey[21,21,21], Dylan B.A. Jones[22,22,22], Nicole S. Lovenduski[23,23,23], Randall V. Martin[24,24,24], Galen A. McKinley[25,25,25], Lesley Ott[26,26,26], Benjamin Poulter[27,27,27], Muye Ru[28,28,28], Stanley P. Sander[2,2,2], Neil Swart[17,17,17], Yuk L. Yung[3,3,3], Zhao-Cheng Zeng[29,29,29], and Junjie LIu[30,30]

[1]Division of Geological and Planetary Sciences California Institute of Technology
[2]Jet Propulsion Laboratory California Institute of Technology
[3]Division of Geological and Planetary Sciences California Institute of Technology
[4]Department of Chemical and Environmental Engineering - Marlan and Rosemary Bourns College of Engineering University of California Riverside
[5]Universities Space Research Association
[6]California Energy Commission
[7]Department of Earth and Planetary Science University of California Berkeley
[8]Department of Mechanical Engineering University of Colorado at Boulder
[9]Department of Climate and Space Sciences and Engineering University of Michigan
[10]Department of Earth System Science Tsinghua University
[11]Jet Propulsion Laboratory, California Institute of Technology
[12]Department of Atmospheric Sciences University of Washington
[13]Milken Institute School of Public Health George Washington University
[14]Modeling and Meteorology Branch California Air Resources Board
[15]Department of Mechanical Engineering University of Colorado at Boulder
[16]Department of Chemistry and Cooperative Institute for Research in Environmental Sciences University of Colorado Boulder
[17]Canadian Centre for Climate Modelling and Analysis Environment and Climate Change Canada
[18]School of Informatics - Computing and Cyber Systems Northern Arizona University
[19]Science and Technology Advancement Division South Coast Air Quality Management District
[20]Department of Environmental Sciences University of California, Riverside
[21]Department of Chemical and Environmental Engineering - Marlan and Rosemary Bourns College of Engineering University of California Riverside
[22]Department of Physics University of Toronto

[23]Department of Atmospheric and Oceanic Sciences and Institute of Arctic and Alpine Research University of Colorado Boulder
[24]McKelvey School of Engineering Washington University in St. Louis
[25]Department of Earth and Environmental Sciences Columbia University
[26]Global Modeling and Assimilation Office NASA Goddard Space Flight Center
[27]Biospheric Sciences Laboratory NASA GSFC Goddard Space Flight Center
[28]The Earth Institute Columbia University
[29]Joint Institute for Regional Earth System Science and Engineering University of California, Los Angeles
[30]NASA Jet Propulsion Laboratory

November 30, 2022

Abstract

The COVID-19 global pandemic and associated government lockdowns dramatically altered human activity, providing a window into how changes in individual behavior, enacted en masse, impact atmospheric composition. The resulting reductions in anthropogenic activity represent an unprecedented event that yields a glimpse into both the past and a future where emissions to the atmosphere are reduced. While air pollutants and greenhouse gases share many common anthropogenic sources, there is a sharp difference in the response of their atmospheric concentrations to COVID-19 emissions changes due in large part to their different lifetimes. Here, we discuss the lessons learned from the COVID-19 disruptions for future mitigation strategies and our current and future Earth observing system.

Societal shifts due to COVID-19 reveal large-scale complexities and feedbacks between atmospheric chemistry and climate change

Joshua L. Laughner[a,1], Jessica L. Neu[b,1], David Schimel[b,1], Paul O. Wennberg[a,c,1], Kelley Barsanti[d], Kevin Bowman[b], Abhishek Chatterjee[e,f], Bart Croes[g,cc], Helen Fitzmaurice[h], Daven Henze[i], Jinsol Kim[h], Eric A. Kort[j], Zhu Liu[k], Kazuyuki Miyazaki[b], Alexander J. Turner[l,h,b], Susan Anenberg[m], Jeremy Avise[n], Hansen Cao[i], David Crisp[b], Joost de Gouw[o,cc], Annmarie Eldering[b], John C. Fyfe[p], Daniel L. Goldberg[m], Kevin R. Gurney[q], Sina Hasheminassab[r], Francesca Hopkins[s], Cesunica E. Ivey[d,t], Dylan B.A. Jones[u], Junjie Liu[b], Nicole S. Lovenduski[v], Randall V. Martin[w], Galen A. McKinley[x], Lesley Ott[y], Benjamin Poulter[z], Muye Ru[aa], Stanley P. Sander[b], Neil Swart[p], Yuk L. Yung[a,b], Zhao-Cheng Zeng[bb], and the rest of the Keck Institute for Space Studies "COVID-19: Identifying Unique Opportunities for Earth System Science" study team[1]

[a]Division of Geological and Planetary Sciences, California Institute of Technology; [b]Jet Propulsion Laboratory, California Institute of Technology; [c]Division of Engineering and Applied Science, California Institute of Technology; [d]Department of Chemical and Environmental Engineering, Center for Environmental Research and Technology, University of California, Riverside, CA 92521, United States; [e]Universities Space Research Association, Columbia, MD 21046, United States; [f]NASA Goddard Space Flight Center, Greenbelt, MD 20771, United States; [g]California Energy Commission, Sacramento, CA 95814, United States; [h]Department of Earth and Planetary Science, University of California, Berkeley, Berkeley, CA 94720, USA; [i]Department of Mechanical Engineering, University of Colorado at Boulder, Boulder, CO 80309 United States; [j]Department of Climate and Space Sciences and Engineering, University of Michigan, Ann Arbor, Michigan 48109, United States; [k]Department of Earth System Science, Tsinghua University, Beijing 100084, China; [l]Department of Atmospheric Sciences, University of Washington, Seattle, WA 98195, United States; [m]Milken Institute School of Public Health, George Washington University, Washington, DC 20052, United States; [n]Modeling and Meteorology Branch, California Air Resources Board, Sacramento, CA 95814, United States; [o]Department of Chemistry, University of Colorado Boulder, Boulder, CO 80309, USA; [p]Canadian Centre for Climate Modelling and Analysis, Environment and Climate Change Canada, Victoria, BC, Canada; [q]School of Informatics, Computing and Cyber Systems, Northern Arizona University, Flagstaff, AZ 86011, United States; [r]Science and Technology Advancement Division, South Coast Air Quality Management District, Diamond Bar, CA, 91765, USA; [s]Department of Environmental Sciences, University of California, Riverside, California, USA; [t]Center for Environmental Research and Technology, Riverside, CA 92521, United States; [u]Department of Physics, University of Toronto, Toronto, Ontario, Canada; [v]Department of Atmospheric and Oceanic Sciences and Institute of Arctic and Alpine Research, University of Colorado, Boulder, CO, USA; [w]McKelvey School of Engineering, Washington University in St. Louis, St. Louis, Missouri 63130, United States; [x]Department of Earth and Environmental Sciences, Columbia University, Lamont Doherty Earth Observatory, Palisades, NY 10964, United States; [y]Global Modeling and Assimilation Office, NASA Goddard Space Flight Center, Greenbelt, MD, United States; [z]Biospheric Sciences Laboratory, NASA GSFC Goddard Space Flight Center, MD, United States; [aa]The Earth Institute, Columbia University, New York, NY 10025, United States; [bb]Joint Institute for Regional Earth System Science and Engineering, University of California, Los Angeles, CA 90095, United States; [cc]Cooperative Institute for Research in Environmental Sciences, University of Colorado Boulder, Boulder, CO 80309, USA

This manuscript was compiled on July 13, 2021

The COVID-19 global pandemic and associated government lockdowns dramatically altered human activity, providing a window into how changes in individual behavior, enacted *en masse*, impact atmospheric composition. The resulting reductions in anthropogenic activity represent an unprecedented event that yields a glimpse into a future where emissions to the atmosphere are reduced. While air pollutants and greenhouse gases share many common anthropogenic sources, there is a sharp difference in the response of their atmospheric concentrations to COVID-19 emissions changes due in large part to their different lifetimes. Here, we discuss two key takeaways from modeling and observational studies. First, despite dramatic declines in mobility and associated vehicular emissions, the atmospheric growth rates of greenhouse gases were not slowed. Second, it demonstrated empirically that the response of atmospheric composition to emissions changes is heavily modulated by factors including carbon cycle feedbacks to CH_4 and CO_2, background pollutant levels, the timing and location of emissions changes, and climate feedbacks on air quality.

COVID-19 | air quality | greenhouse gases | Earth system | mitigation

The effects of the COVID-19 pandemic and associated lockdown measures have provided a way to observationally test predictions of future atmospheric composition. This is illustrated conceptually in Figure 1. With many people working from home and limiting travel, the pandemic caused a significant decrease in anthropogenic emissions. These emissions reductions can be thought of as a jump forward in time to a future where additional systemic emissions controls have been adopted. However, because these changes occurred in a matter of months, the changes to the concentrations of key air quality (AQ) and climate relevant gases in the atmosphere were readily observable. Combining these observations with current state-of-science models allows us an important window into the underlying processes governing the response of the Earth system to reductions in anthropogenic emissions, and thus a preview of the relative effectiveness of different emissions control strategies.

Our goal is to synthesize some of the key results from the past year into a coherent understanding of what we have learned about the effectiveness of different strategies to reduce greenhouse gas (GHG) emissions and improve AQ. We will do so in four parts. First, we summarize the observed changes

Significance Statement

The COVID-19 pandemic and associated lockdowns caused significant changes to human activity that temporarily altered our imprint on the atmosphere, providing a brief glimpse of potential future changes in atmospheric composition. This event showed key differences in how air quality and atmospheric greenhouse gas concentrations respond to changes in anthropogenic emissions, with implications for future mitigation strategies.

JLL led the manuscript and the human activity analysis. JN, DS, and POW led the study team. K. Barsanti, K. Bowman, DS, AT, and EK led study subgroups. Remaining authors contributed data analysis. All authors helped revise the manuscript.

The authors declare no competing interests.

[1]To whom correspondence should be addressed. E-mail: jlaugh@caltech.edu, jessica.l.neu@jpl.nasa.gov, david.schimel@jpl.nasa.gov, or wennberg@gps.caltech.edu

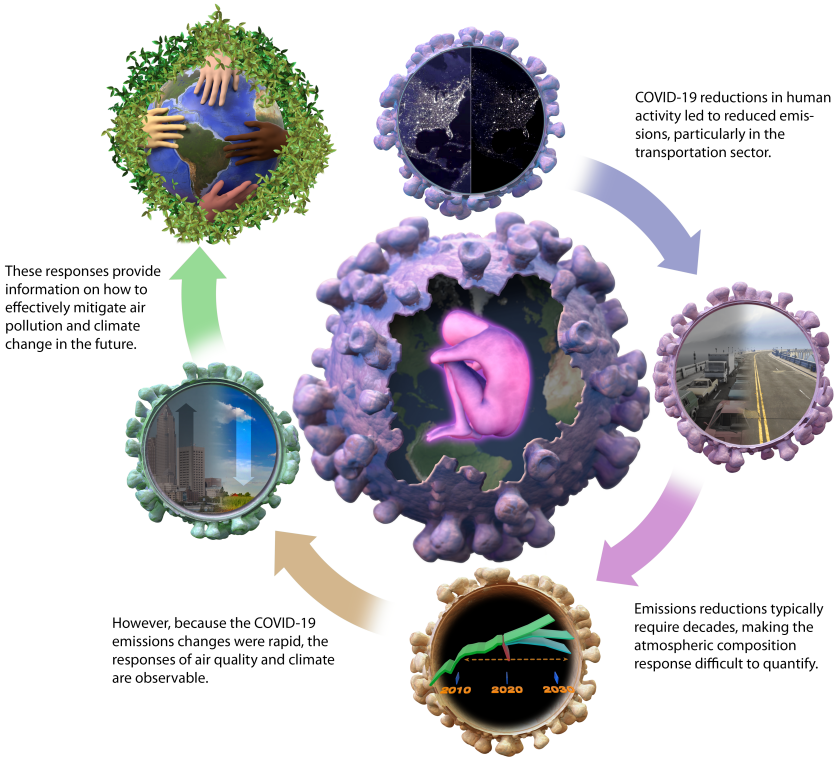

Fig. 1. Illustration of the conceptual foundation for this study. The COVID-19-induced reductions in human activity led to reduced anthropogenic emissions. The fact that these reductions occurred over months rather than decades allows us to observe how the atmosphere, land, and ocean are likely to respond in a future scenario with stricter emissions controls. This analysis helps to identify effective pathways to mitigate air pollution and climate change. Image credit: Chuck Carter / Keck Institute for Space Studies

in anthropogenic emissions during 2020. Second, we examine how the reduction in CO_2 emissions impacted the atmospheric CO_2 growth rate. Third, we show that the response of AQ to emissions reductions is very spatially heterogeneous, and summarize the causes of that heterogeneity. Fourth, we discuss the implications of these results for future AQ improvement strategies, our understanding of processes controlling GHG concentrations in the atmosphere, feedbacks between AQ, GHGs, and climate, and finally close by identifying strengths and gaps in our current observing networks. We draw three primary conclusions from this synthesis:

1. Despite drastic reductions in mobility and resulting vehicular emissions during 2020, the growth rates of GHGs in the atmosphere were not slowed.

2. The lack of clear declines in the atmospheric growth rates of CO_2 and CH_4, despite large reductions in human activity, reflect carbon cycle feedbacks in air-sea carbon exchange, large interannual variability in the land carbon sink, and the chemical lifetime of CH_4. These feedbacks foreshadow similar challenges to intentional mitigation.

3. The response of AQ to emissions changes is heavily modulated by factors including background pollutant levels, the timing and location of emissions changes, and climate-related factors like heat waves and wildfires. Achieving robust improvements to AQ thus require sustained reductions of both AQ and GHG emissions.

Summary of emissions in 2020

As AQ-relevant gases and CO_2 are co-emitted by combustion processes, decreases in human activity are expected to drive decreases in both of these species. Figure 2 summarizes changes to key sectors of human activity during the COVID-19 pandemic. Figure 2a shows the Oxford Stringency Index (1), which quantifies the severity of government-imposed restrictions on travel, businesses, schools, and other aspects of society. Panels b, c, and d show changes in air travel & maritime shipping, traffic, and United States (US) electricity use, respectively. There is a clear decrease in air travel and traffic for most of the world in March 2020, when the first major wave of COVID-19 led governments to institute quarantine measures (see also high values of the Stringency Index). Maritime shipping (to west coast US ports) and power generation (in the US) were less affected. Power generation in particular remained within approximately 5% of 2019 levels.

Reductions in NO_x emissions were apparent in both in situ (5) and satellite (6) observations of NO_2 concentrations due to the short atmospheric lifetime of NO_x ($<$ 1 day). Estimates of NO_x emissions reductions from assimilating satellite data in global models (7), combining global chemical models with machine learning trained on surface measurements (8), or activity data (including electricity use, traffic/mobility data, flight data, etc.) (9–11) find regional reductions of 10% to 40% during the strictest lockdown periods. Generally, methods assimilating satellite data report smaller reductions (10% to 20%) than studies based on activity data (25% to 40%).

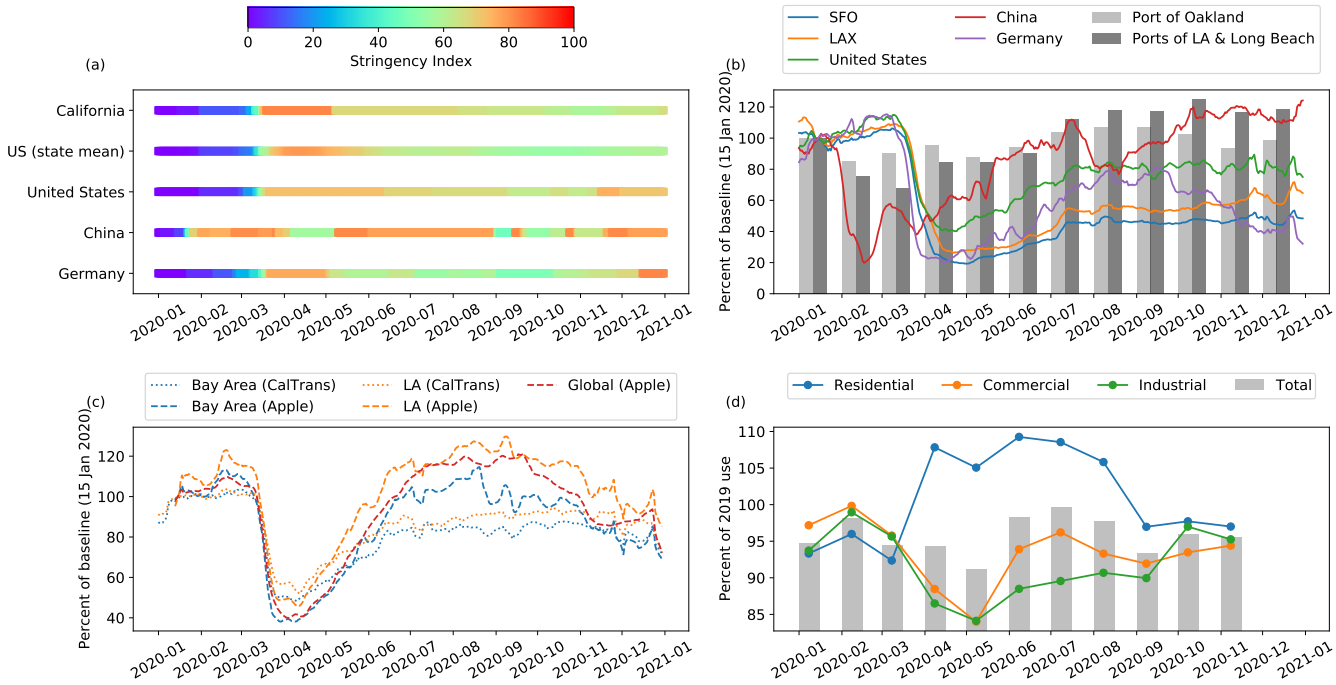

Fig. 2. Metrics for change in human activity at different scales show that the strongest impact of COVID-19 lockdowns were in the transportation sections, and that these impacts varied substantially from country to country. Panel **(a)** shows the Oxford stringency index (1) for the regions used in this figure. "US (state mean)" is the average of individual states' indices, "United States" is the index attributed to the US as a whole (not individual states, see SI for discussion). Panel **(b)** shows the percent change in flights (2–4) for two California airports and three countries (lines) and container moves for three California ports (bars) Panel **(c)** shows traffic metrics for two California urban areas, and 26 countries ("global"). CalTrans indicates Caltrans PEMS data; Apple indicates Apple driving mobility data. Panel **(d)** shows electricity consumption in the US by sector, relative to the same month in 2019. The three sectors shown constitute $> 96\%$ of US power consumption. In **(b)** and **(c)**, daily metrics are relative to 15 Jan 2020 and presented as 7 day rolling averages and monthly metrics are relative to Jan 2020. Electricity consumption not available after Nov 2020 at time of writing.

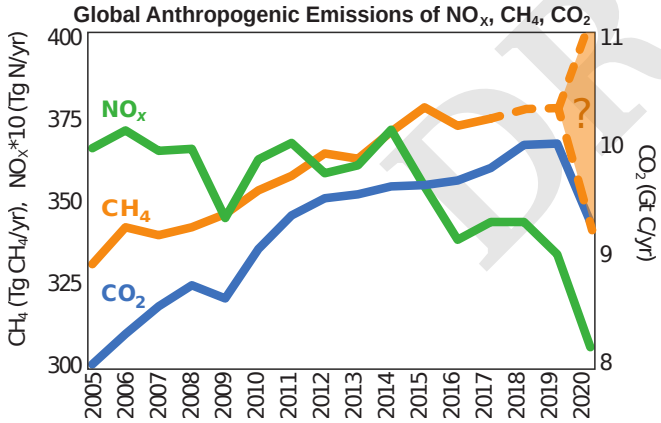

Fig. 3. 2020 saw reductions in CO_2, CH_4, and NO_x emissions. CH_4 and NO_x are plotted along the left axis, CO_2 on the right. The dashed line for CH_4 after 2017 indicates it is estimated from the average rate of increase. 2020 emissions are represented as a range: the IEA estimated a 10% decrease in CH_4 emissions in 2020(12), but this is uncertain, as the CH_4 growth rate increased in 2020. Full details are in the SI.

Estimates of the reduction in global NO_x emissions in the first half of 2020 range from 5% (8) to 13% (7).

The change in global CO_2 emissions was comparable to that of NO_x emissions, as seen in Fig. 3. Liu et al. report a peak global reduction of approximately 15% (4 Tg C or 15 Mt CO_2) in April, and an annual total of 5.4% (13). In March 2020, Le Quéré et al. projected a slightly larger 7% decrease in CO_2 over the remainder of 2020 (14). The largest decreases occurred in the first half of 2020, as shown in Fig. 4a and were primarily associated with reductions in ground transportation (15). The response of atmospheric CO_2 mixing ratios can be observed near the emissions sources; during the strictest lockdowns, Turner et al. were able to use CO_2 observations from a local ground-based network to estimate a 48% reduction in traffic CO_2 emissions in the San Francisco Bay Area (16). Liu et al. found a 63% (41 ppm) decrease of the typical on-road CO_2 enhancement in Beijing, China (17). Distinguishing these signals in CO_2 at regional scales is more challenging. Buchwitz et al. infer peak decreases in anthropogenic CO_2 emissions from China of 10% from space-based total column CO_2 measurements (18). However, they note that the uncertainty is approximately 100%, and that the expected CO_2 concentration signal is 0.1 to 0.2 ppm, out of a background of over 400 ppm.

Anthropogenic CH_4 emissions are dominated by sources such as landfills, oil and gas production, and agricultural activities. The International Energy Agency (IEA) estimates that CH_4 emissions dropped by 10% in 2020 (Fig. 3), largely due to the decrease in demand for oil and gas. However, it is unclear whether reduced demand during 2020 was the primary driver of emissions. It is likely that decreased maintenance of landfills and oil and gas infrastructure during the COVID-19 pandemic led to new leaks in some areas, which can result in those locations becoming CH_4 "superemitters" (19). In general, the type, maintenance level, and throughput of CH_4 infrastructure can have a large impact of the amount of fugitive

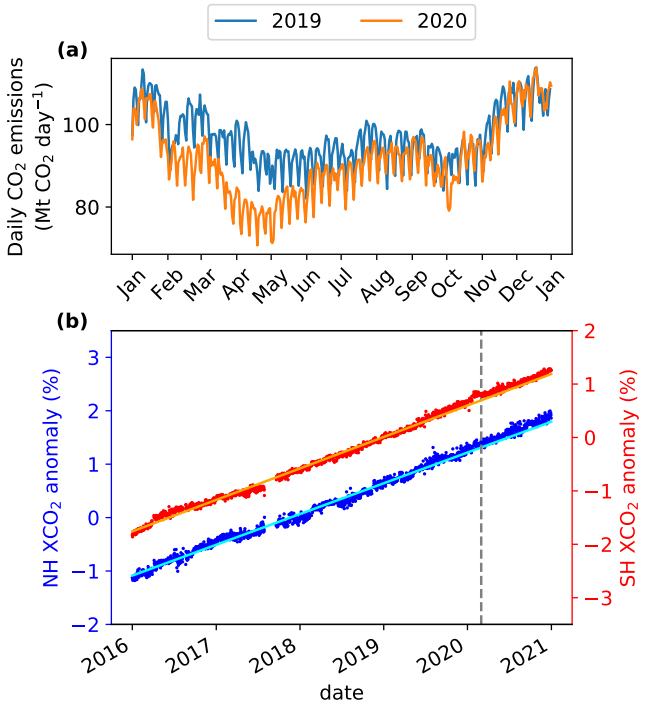

Fig. 4. Despite substantial reductions in anthropogenic CO_2 emissions in early 2020, the annual atmospheric CO_2 growth rate did not decline. Panel **(a)** shows daily global CO_2 emissions for 2019 and 2020, calculated following Liu et al. (13). Panel **(b)** shows trends in atmospheric column average CO_2 from the Orbiting Carbon Observatory 2 (OCO-2). The small blue and red symbols indicate daily, deseasonalized values as percent anomalies relative to the global 2018 mean. The solid cyan and orange lines are linear fits to 2016 through 2019 data. In panel (b) the vertical gray dashed line marks 1 March 2020 as the approximate beginning of lockdowns in response to COVID-19. A version of (b) showing the absolute trends and the data including the seasonal cycle is available as Fig. S8 in the SI.

emissions (20, 21). On a positive note, some of the decrease in emissions estimated by the IEA was associated with the installation of new oil and gas infrastructure and the adoption of new CH_4 regulations in a number of countries (12). Such decreases would likely be sustained beyond the pandemic period.

CO_2 and CH_4 atmospheric growth rates

The effect of CO_2 emissions reductions, especially from ground transport, were clearly apparent in urban-scale observations of atmospheric CO_2 mixing ratios (16, 17). This does not, however, transfer to global-scale observations. Figure 4b shows deseasonalized trends in column-average CO_2 mixing ratios (referred to as XCO_2) observed by the Orbiting Carbon Observatory 2 (OCO-2) instrument. Despite the reduction in CO_2 emissions in 2020 (Fig. 4a), there is no clear deflection of the observed XCO_2 below what would be projected based on previous years' growth rates. We compared the variability in actual atmospheric CO_2 growth rates derived from the OCO-2 data with that computed from fossil fuel emissions (Fig. S8b) and found that the change in atmospheric CO_2 growth caused by the COVID-19 pandemic is smaller than the natural year-to-year variability. This is expected, because the percent change in the CO_2 growth rate, in the absence of feedbacks, will match the percent change in emissions. For a typical

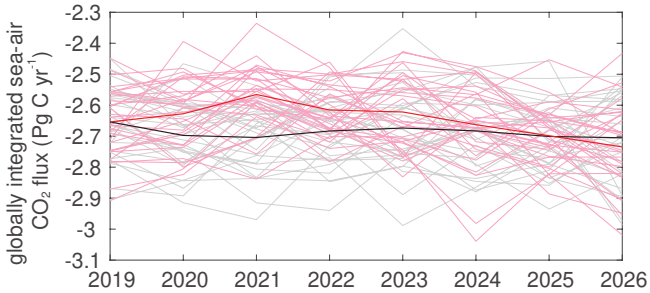

Fig. 5. Sea-air carbon exchange responded quickly to the reduction in anthropogenic CO_2 emissions during 2020. Shown here are annual mean, globally integrated sea-to-air carbon dioxide fluxes predicted from the CanESM5-COVID ensemble (24, 25). Black/gray lines derive from simulations forced with SSP2-RCP4.5 CO_2 emissions, while red/pink lines derive from simulations forced with a 25% peak CO_2 emissions reduction in 2020. See (24, 25) for more details. Thick lines are ensemble averages, and thin lines are individual ensemble members, each with different phasing of internal variability.

growth rate of 2.45 ppm/year since 2016 (Fig. S8b and 22), the 5.4% total reduction in CO_2 emissions calculated by Liu et al. (13) equals a 0.13 ppm/yr decrease in the CO_2 growth rate for 2020—well within the natural variability observed by OCO-2 (Fig. S8) and surface networks (22).

Wildfires are one element of the variability in CO_2 growth rate. The 2019/2020 Australian wildfires emitted 173 Tg C (634 Mt CO_2) between Nov 2019 and Jan 2020, over 6 times more than Australia's average Nov.-Jan. CO_2 emissions for 2001 through 2018 (23). This drove an early increase in CO_2 in 2020, evident in the deseasonalized southern hemisphere OCO-2 XCO_2 (Fig. 4b, red series) and growth rate derived from the OCO-2 data (Fig. S8b). This wildfire anomaly offset a third of the 518 Tg C (1901 Mt CO_2) reduction in anthropogenic CO_2 (13) and so does not fully explain the offset between emissions and atmospheric mixing ratios for CO_2.

The atmospheric CO_2 growth rate led to a reduction in the rate of oceanic CO_2 uptake. Figure 5 shows the magnitude of ocean carbon fluxes over 8 years as computed from a model ensemble under normal and COVID-like emissions. There is significant variation in the sea-air and CO_2 flux among the model ensemble members. This spread represents the potential interannual variability in CO_2 flux; given that variability, the true change in CO_2 flux in 2020 is uncertain, in part due to corresponding variability in the land carbon sink (Fig. S9). However, the ensemble mean indicates that while on short time scales the land carbon flux is insensitive to the change in emissions (Fig. S9), the ensemble mean ocean uptake was reduced by 70 Tg C/yr in 2020. This would offset 14% of the approximately 520 Tg C/yr (1901 Mt CO_2/yr) reduction in anthropogenic CO_2 emissions in 2020 (13), further dampening the signal from emissions reductions in atmospheric CO_2.

The growth rate of CH_4 was also not slowed by the pandemic. Figure 6a shows trends in column average CH_4 (XCH_4) from two ground based spectrometers in the Total Carbon Column Observing Network (TCCON, 26, 27) located in Park Falls, Wisconsin, US (28) and Lauder, New Zealand (29, 30). The XCH_4 values after 1 March 2020 lie approximately 0.3% above the 2016 to 2019 trend in both hemispheres. Similarly, NOAA reported the single largest increase in CH_4 in its record (31).

Because the lifetime of CH_4 depends on the abundance of

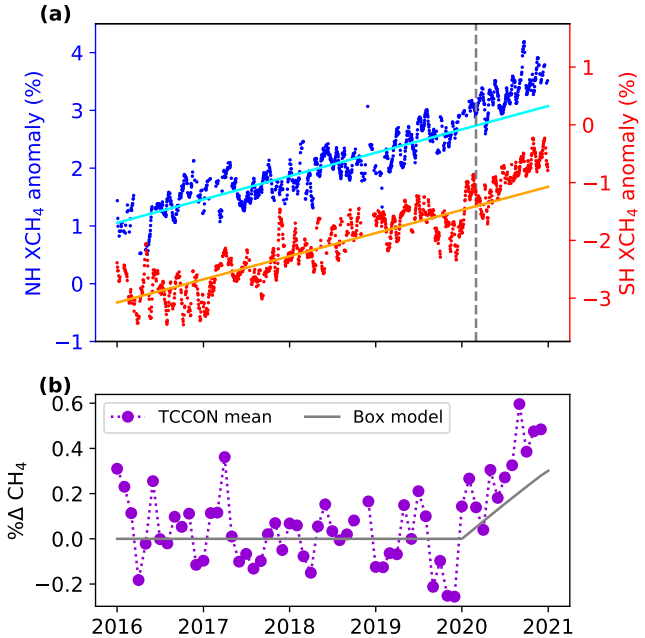

Fig. 6. Atmospheric mixing ratios of CH_4 increased more rapidly in 2020 than they had in the past decade. The increase is consistent with no change in CH_4 emissions and a 3% decrease in OH (predicted from decreased NO_x emissions) during 2020. Panel **(a)** is similar to Fig. 4b, except it shows trends in column-average CH_4 (XCH_4) from two TCCON sites: Park Falls, WI, USA in the northern hemisphere and Lauder, New Zealand in the southern hemisphere instead of OCO-2 XCO_2. Panel **(b)** compares the TCCON XCH_4 trend to that predicted by a box model. The purple series are the monthly mean percent differences between the TCCON XCH_4 and linear fits from (a). The grey line represents the percent difference in CH_4 predicted by a box model (33) with a 3% decrease in OH during 2020 compared to no change in 2020 OH.

the hydroxyl radical (OH), the concentration of CH_4 varies with atmospheric pollution levels. In fact, we find compelling evidence that the jump in CH_4 mixing ratios during 2020 is partly due to reductions in NO_x emissions. In a model incorporating the decreased NO_x emissions associated with COVID-19 (32), the resulting decrease in global ozone (7) leads to a 2% to 4% decrease in global OH concentrations. As oxidation by OH is the primary loss process for atmospheric CH_4, this acts to increase CH_4 mixing ratios in the atmosphere. Figure. 6b compares the trend in XCH_4 measured by TCCON to that predicted by a box model (33). The purple series is the monthly percent difference of TCCON XCH_4 from the linear trends shown in Fig. 6a, and the gray line is the percent difference between a box model run with and without a 3% decrease in OH during 2020. The box model closely matches the extra growth in atmospheric CH_4 during 2020, indicating that the change in OH was an important driver of the observed CH_4 growth. However, this is inconsistent with the 10% decrease estimated by the IEA (12), as our box model assumes constant CH_4 emissions after 2012.

If decreases in anthropogenic NO_x emissions during 2020 were responsible for the increase in CH_4 lifetime that led to its higher than expected growth rate, what does this imply for the effect of future efforts to reduce NO_x emissions to improve AQ? To understand this, we need to examine how the 2020 NO_x decreases affected AQ around the world. In the next section, we will describe the ozone and particulate matter (PM) response to these NO_x reductions. Afterward, we will explore the implications of this AQ-GHG in the discussion.

Heterogeneity in air quality response

Most parts of the world saw significant decreases in NO_x emissions during the pandemic, but the magnitude and timing of these emissions changes varied with location. Figures 7a-c compare timeseries of NO_2 column densities measured by TROPOMI for three cities. Following the beginning of lockdown measures (indicated by the dotted lines), the 2020 NO_2 column densities are clearly less than in 2019. However, in Los Angeles, the drop in NO_2 occurred very rapidly when lockdowns were enacted in early March, but by May there was little difference between 2019 and 2020. In Lima, on the other hand, the difference between 2019 and 2020 grew from March through May. In Shanghai, we see a very large drop in NO_2 associated with the early lockdown in January and a smaller drop during the second lockdown in late February.

These changes in NO_x emissions drove changes in secondary pollutants, such as ozone and PM. However, the ozone and PM responses depended on the local chemical regime and meteorology, as well as the magnitude and timing of the NO_x emissions reductions. In this section, we describe the factors controlling the ozone response first, followed by PM.

Ozone. Ozone is a secondary pollutant produced in the atmosphere from the reaction of NO_x and OH with volatile organic compounds (VOCs). The response of ozone concentrations to changes in NO_x emissions is characterized by the ozone production efficiency (OPE), which is the ratio of the change in ozone for a given change in NO_x.

Figures 7d-f show the ozone production efficiency (OPE) calculated in a global model that assimilates multiple satellite measurements. The OPE values shown represent the change in ozone mass burden per unit change in mass of reactive nitrogen emissions, using the COVID-19 reduction in emissions as the ΔNO_x. More detail is given in the SI.

Two patterns in the OPEs demonstrate the significant spatial and temporal variability in the relationship between NO_x emissions and ozone concentrations. First, in Fig. 7f, the OPE in the Northern hemisphere increases between February and June. This is mostly due to increasing sunlight driving key photolysis reactions more rapidly. Thus, the timing of NO_x emissions changes plays a significant role in the magnitude of the ozone response in the mid- and high-latitudes, with a smaller ozone response to a given NO_x change during spring than during summer. Second, in Fig. 7d, tropical and subtropical cities have the largest, most positive OPEs. Furthermore, there is little change in OPE with season for these cities (Fig. 7e) due to the relatively small changes in insolation at low latitudes. Figure 7d indicates that most of the northern mid-latitude cities have small, positive OPEs. Two cities, however, have slightly negative OPEs (Beijing -0.10, Karachi -0.06); a negative OPE indicates that ozone increased when NO_x emissions decreased. Other studies have, in fact, identified large ozone increases in China (34) associated with the decreased NO_x emissions during the pandemic. Additional increases in ozone were observed in Europe (35), with smaller but still positive changes in ozone in the United Kingdom (36).

We use a steady-state model (Fig. S10) to interpret the patterns in Fig. 7. From the steady-state model, we know OPE is small at both low and high NO_x concentrations, but large at

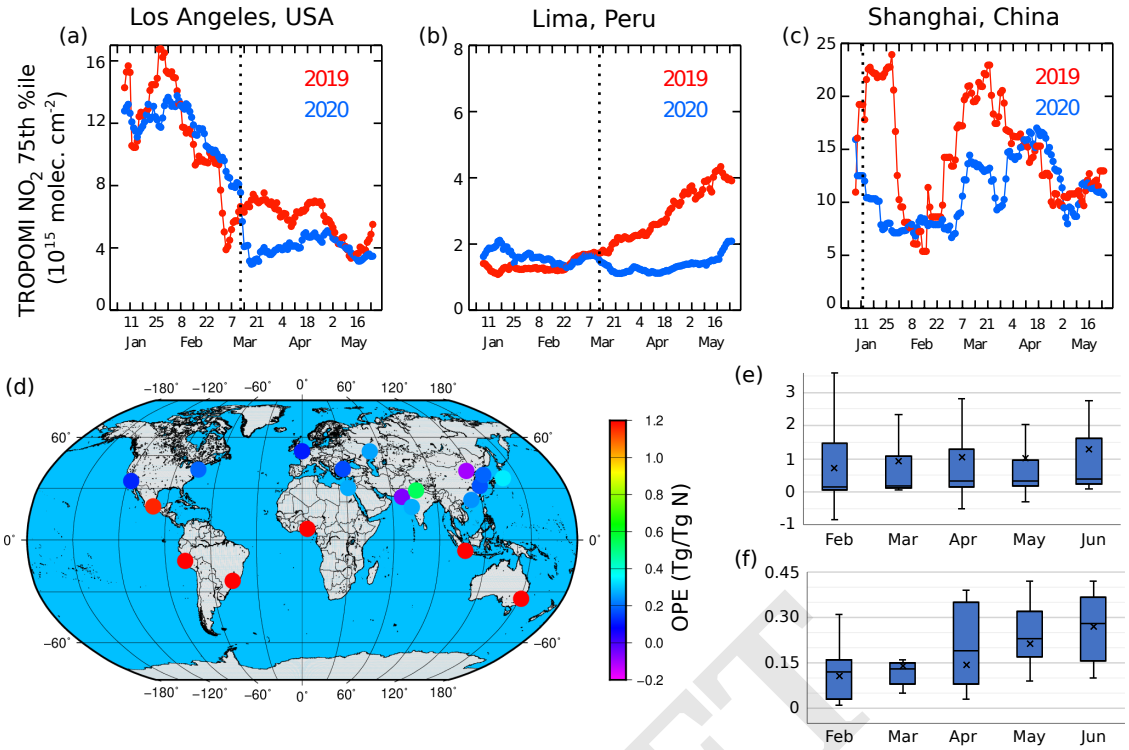

Fig. 7. COVID-19 lockdowns dramatically reduced urban NO_2 levels, which in turn drove changes in O_3 production. Panels **(a–c)** show 15 day rolling averages of 75th percentile TROPOMI NO_2 column densities in three cities for 2019 and 2020. The vertical dotted line indicates the beginning of lockdown measures in 2020. Panel **(d)** shows OPE modeled in 17 megacities, averaged from February to June 2020. Panel **(e)** shows modeled monthly global averaged tropospheric O_3 production efficiency (OPE). The whiskers are the minimum and maximum, the horizontal lines the quartiles and median, and the X is the mean. Panel **(f)** is similar to (e), but averaged over 30° N to 90° N.

intermediate NO_x concentrations. Overall OPE also increases with VOC reactivity (VOC_R, the total rate of reaction of all VOCs with OH in a given parcel of air) for NO_x concentrations greater than ~ 0.1 ppb. Thus, in Fig. 7, areas with negative OPE are in the high-NO_x part of the OPE curve; sustained efforts to reduce NO_x emissions will bring them closer to the maximum-OPE tipping point, after which NO_x reductions should lead to ozone reductions. Cities in the tropics and subtropics have large, positive OPE values. This is partly due to plentiful sunlight to drive photochemistry, but these regions also have large VOC_R values due to the abundance of biogenic VOCs (37). The steep dependence of OPE on NO_x follows because NO_x is the limiting reactant in ozone production in these high-VOC_R conditions. Thus, these cities should see large ozone reductions from NO_x reductions. However, of the equatorial cities shown in Figure 6, only those located in South Asia had large enough reductions in NO_x emissions during the COVID-19 pandemic to produce substantial reductions in surface ozone (3-5 ppb) (7).

We also see this heterogeneity in ozone response to NO_x emissions reductions at the intraurban scale. Measurements of daily maximum NO_2 and ozone at monitoring sites throughout the Los Angeles Basin show consistent reductions in NO_2 throughout the basin in March and April of 2020, but smaller reductions in ozone in the central northern part of the basin than elsewhere (Figs. S1, S2). This is consistent with the near-0 OPE for Los Angeles in Fig. 7d, i.e. for a city on the verge of reducing NO_x emissions to the point where NO_x is the limiting factor in ozone production. While the overall basin chemistry is at this tipping point, local differences in emissions as well as transport of pollutants within the basin can lead to these small scale differences in ozone response (38).

However, the behavior of ozone in the Los Angeles Basin also illustrates that NO_x controls may become less effective in a warmer climate. Figure 8 shows time series of daily maximum NO_2 and ozone (top and middle panels). NO_2 and ozone concentrations are clearly lower in March and April 2020 compared to the 2015 to 2019 average, in part due to the reduction in NO_x emissions at the beginning of the lockdown. However, these two months were significantly cooler than the 2015 to 2019 average as well. When temperatures rose above average during an unusual heat wave in late April and May of 2020, ozone daily maxima rose above the range seen in 2015 to 2019, despite the fact that NO_2 remained similar to 2015 to 2019 concentrations. An increase in ozone during April and May was also seen in a previous study (39). The response of ozone per degree increase in temperature is shown in Fig. S3. Typical values for the O_3 season (May-Sep) in 2020 throughout the basin were 1.8 to 5.8 ppb K^{-1} . This is higher than a previous prediction of about 1 ppb K^{-1} in the basin (40), suggesting the ozone climate penalty may be stronger than expected; however, analysis is ongoing.

Particulate matter. Achieving long-term reductions in PM (especially PM 2.5, particles with a diameter $< 2.5\mu$m) concentrations is a matter of great importance due to the large health impacts of PM compared to ozone (41). Our interest here is to use observations from the pandemic period to better understand some of the factors controlling atmospheric PM concentrations, rather than focusing on the question of whether

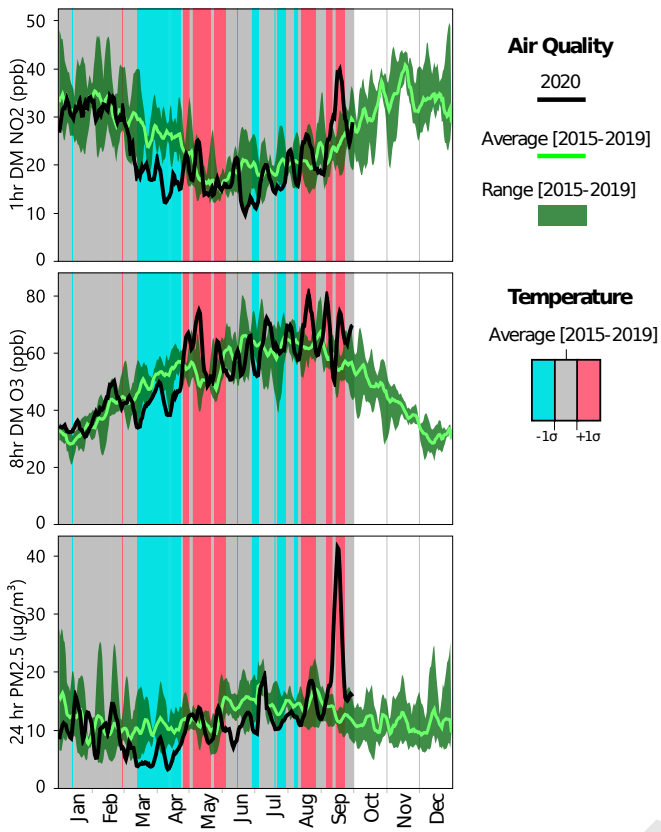

Fig. 8. In Los Angeles, temperature and wildfires drove ozone and PM pollution, respectively, more than changes in traffic. The three panels show 7-day rolling average of 24hr $PM_{2.5}$, 1hr daily maximum (DM) NO_2, and 8hr DM O_3, respectively, by day of year in 2020 and in the past five years (2015-2019) in the LA Basin. Bars in the background show the 7-day rolling average of basin-average 1 hr DM temperature in 2020 relative to the 2015 to 2019 average ($\pm 1\sigma$) by day of year. 2020 data are preliminary, unvalidated, and subject to change.

PM exposure increases the chance of death from COVID-19.

The factors controlling PM concentration are more complicated than those for ozone. PM arises from primary emissions and natural sources, as well as secondary chemistry in the atmosphere. One such secondary pathway is the formation of nitrate PM from the reaction of higher oxides of nitrogen (such as HNO_3) with ammonia (42). Nitrate PM formation via this pathway may be limited by either available NO_x or ammonia.

Model simulations (Fig. S4) demonstrate the effect that NO_x emissions reductions had on nitrate PM formation in Los Angeles. Under COVID-19 emissions, the nitrate PM concentrations decreased by approximately 60% in April 2020. At the same time, the model reported a shift towards NO_x-limited (rather than ammonia-limited) chemistry. This implies that the NO_x emissions decreases in April, when the shift in the chemical regime shows the largest change, were more efficient at reducing nitrate than the reductions in other months. Compared to the measured total PM reductions shown in the bottom panel of Fig. 8, our results suggest that NO_x emissions reductions account for about 10% of the total PM reduction in the Los Angeles Basin during the COVID-19 lockdowns. This agrees with other recent work (43) which indicate that traffic NO_x emissions contribute less than 10% of secondary PM production throughout North America, Europe, and East Asia.

The relative availability of NO_x and ammonia elsewhere in the US plays an important role in whether NO_x emissions reductions lead to reduced nitrate PM. Simulations of nitrate chemistry over the continental US show that Los Angeles is somewhat unique as an urban area that experienced a significant shift to NO_x-limited nitrate chemistry. Other urban areas in the northeast, southeast, and northwest largely remained ammonia-limited (Figs. S5–S7). This could explain, at least in part, the scattered response of PM to NO_x emissions reductions across US cities seen in other studies (44). It also implies that continuing the long-running trajectory of NO_x emissions reductions in Los Angeles in order to reach the tipping point where ozone becomes NO_x limited will also benefit AQ via reduced production of nitrate PM.

However, Los Angeles also represents a cautionary tale about attributing AQ changes to the COVID-19 pandemic without accounting for other confounding factors. Weather and wildfires also played a large role in determining the PM concentrations in Los Angeles during 2020. When the lockdowns were first instituted in March, news outlets and social media attributed the clean air in the Los Angeles Basin to the lack of traffic. However, as seen in Fig. 8, the lower PM concentrations in March and April 2020 than 2015 to 2019 (Fig. 8, bottom) coincide with anomalously cool weather, which was accompanied by higher than average precipitation (Fig. S1 in (38)). Precipitation removes PM from the atmosphere through wet deposition (45, 46), and was at least partially responsible for the clean air during this period. The extreme spike in PM concentrations seen in September 2020, on the other hand, coincides with a time period when major wildfires were burning in close proximity to Los Angeles. Like the April-May heatwave, this event also points to the fact that climate change can erase progress in AQ improvement through emissions reductions.

Discussion

The changes in atmospheric composition throughout 2020 unequivocally demonstrate that AQ and GHGs cannot be treated as separate problems, despite the disparate time scales of AQ and GHG responses to changes in human activity. AQ is most dependent on local changes in emissions because of the shorter atmospheric lifetime and rapid chemistry of AQ-relevant pollutants. In contrast, the global total GHG emissions matter more than local emissions, as it is the overall GHG atmospheric growth rate that drives climate change. As discussed above, improvements in AQ made by reducing pollutant emissions locally can be offset by changes in meteorology or non-anthropogenic (e.g. biogenic or wildfire) emissions driven by climate change. Likewise, changes in AQ can affect climate change, as decreases in AQ-relevant emissions could lead to increased lifetimes for shorter-lived GHGs (such as CH_4), increasing their global warming potential.

Reductions in NO_x emissions during the pandemic did show the potential benefits cities can gain by promoting systemic change to accomplish these same reductions. For most countries, the pandemic-induced emissions reductions can be seen as going back in time to a period when NO_x emissions were lower. In the US, Europe, and China, where NO_x emissions have been trending downward, these reductions were more

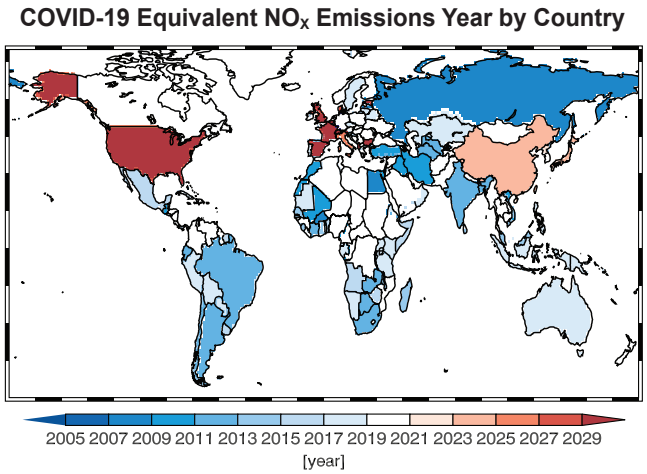

Fig. 9. The emissions reductions during the pandemic are, in a sense, like moving forward or back in time. Countries are colored by the year to which their 2020 NO_x emissions are equivalent, projected forward in time where emissions have been decreasing and backward elsewhere. Details of emissions estimates given in the SI.

akin to a jump forward in time to a lower emissions future. Figure 9 shows the equivalent year for each country's NO_x emissions during the pandemic, assuming recent trends in NO_x emissions hold constant. Most striking is how much more quickly China could reach pandemic-like emissions levels than the US or Europe. Though all three regions' emissions reductions had similar peak magnitudes (18% to 20%), Europe and especially the US are further along their respective NO_x reduction pathways than China. This, combined with China's higher pre-pandemic emissions levels, means that China can make progress quickly if they are able to maintain the aggressive pace of emissions reductions they have set over the past decade (32).

Many cities in the US and Europe are close to reaching a point at which NO_x emissions will be a very effective control on ozone concentrations. In Fig. 7d, cities with an OPE near 0 are likely at the tipping point between VOC-limited and NO_x-limited chemistry. Further NO_x reductions should move them firmly into NO_x-limited chemistry, where NO_x is the primary control on ozone formation. While sustaining these emissions reductions may be challenging due to the decreasing contribution of on-road gasoline emissions (47) and the impact of emissions reductions being offset in part by increases in chemical lifetime (48), the rewards in doing so are likely substantial. In addition, since NO_x and CO_2 are co-emitted by combustion processes, regulations such as those that encourage a transition to electric vehicles will also benefit climate. In fact, recent work has shown that the cost savings associated with reduced health impacts from air pollution will outweigh the cost of transition to a clean carbon economy and that the increased radiative forcing from longer-lived CH_4 and ozone is balanced by the decrease in forcing from smaller CO_2 mixing ratios (49). On the other hand, measures such as NO_x removal from coal-fired power plants will benefit AQ but not climate; as discussed below, this will eventually limit their effectiveness for improving AQ.

The same strategies to improve AQ will not be equally effective in all locations. On one hand, the tropical and subtropical cities with large, positive OPE values in Fig. 7d can immediately realize substantial ozone reductions through reductions in NO_x emissions. On the other hand, cities such as Beijing and Karachi with negative OPEs, or locations such as the United Kingdom where in situ studies found a negative correlation between NO_x emissions and ozone concentrations (36) would do better to reduce volatile organic compound (VOC) reactivity simultaneously with NO_x emissions. Such an approach would allow them to avoid the chemical regimes with the largest OPEs (50) (Fig. S10a). Similarly, while chemical formation of ammonium nitrate PM in Los Angeles became NO_x-limited during the pandemic, most other cities in the US remain ammonia-limited and would see stronger reductions in PM by controlling primary emissions, organic precursors, or other key species.

Unfortunately, 2020 has also shown that improvements in AQ are likely to be offset by climate feedbacks. Such effects were most apparent in Los Angeles, where warmer than average May temperatures led to ozone concentrations above the 2015 to 2019 average, greater than average precipitation in March and April likely contributed to the reduction in PM, and severe wildfires from late August through September caused PM concentrations four times that of the 2015 to 2019 average. Changing climate will affect each of these variables, leading to warmer temperatures, more wildfires (51), and potentially more intense but less frequent precipitation (52), giving PM more time to accumulate between wet deposition events.

Changes in AQ-relevant emissions, particularly NO_x emissions, have potential to feed back into climate change as well. As we showed in Fig. 6, there is compelling evidence that reductions in OH stemming from reduced anthropogenic NO_x emissions drove a $\sim 0.3\%$ jump in CH_4 during 2020. While tropical cities have the greatest potential for decreasing ozone by reducing NO_x emissions (Fig. 7d), they also have an outsized impact on atmospheric CH_4 lifetime, as the largest share of CH_4 oxidation occurs in the tropics (33). Since only tropical cities in South Asia had substantial changes in NO_x emissions during 2020 (7), 2020 represents a minimum benchmark for the effect of NO_x reductions on the CH_4 growth rate. It is therefore essential to invest strategies to reduce fugitive CH_4 emissions (such as updated CH_4 storage and transportation infrastructure to prevent and limit leaks, landfill CH_4 capture, and confined animal feed operation CH_4 mitigation) ahead of decreases in tropical NO_x emissions.

In terms of climate, despite a reduction in global emissions equivalent to going back in time nine years (to 2011-equivalent CO_2 emissions), any change to the global CO_2 growth rate was smaller than typical interannual variability. As mentioned earlier and discussed in more detail below, this is partly due to the offsetting reduction in ocean carbon uptake (Fig. 5), but also arises because the sharp decreases in CO_2 emissions during the first half of 2020 were not sustained. By the second half of 2020, emissions due to power generation, industry, and residential consumption had nearly returned to 2019 levels (13). If we assume that these emissions levels represent a balance between reduced activity to limit the spread of COVID-19 and sufficient activity to maintain a minimum economic productivity, this suggests that reducing activity in these sectors is not practical. Reducing these sectors' emissions permanently will require their transition to low carbon emitting technologies.

One interesting aspect of the GHG emissions reductions during the pandemic was that they provided a chance to study

the feedback in ocean carbon uptake. The model simulations using COVID-like CO_2 emissions shown in Fig. 5 indicate that the sea-air carbon flux adjusts rapidly in response to changes in anthropogenic emissions. That model ensemble mean indicates a response time of about one year. Though this basic response - a decline of the ocean carbon sink in response to mitigation - is accounted for the RCP scenarios (53), much uncertainty remains as to the accuracy of these ocean sink predictions. This uncertainty is due both to the forced response of the ocean and to interannual variability Lovenduski et al. found that, for a change in ocean carbon uptake to be observable with our current network of ocean buoy measurements, it would need to be four times larger than the COVID-19 emissions reductions (25). This will be a challenge as we work to quantify the effect of future permanent CO_2 emissions reductions on atmospheric CO_2 mixing ratios.

The pandemic does offer insight into how the atmospheric GHG growth rates could be curtailed: systemic changes are required to enable sustained reductions in emissions. The efficacy of sustained reductions (without systemic changes to the energy sector) can be seen in the contrast between CO_2 emissions from ground transport and international shipping and aviation ("international bunkers") reported by Liu et al. (13) The peak reduction in international bunkers' emissions was only approximately 1/3rd that of the reduction in emissions from ground transport, by mass. However, while ground transport recovered fairly quickly, the international bunkers' emissions remained at about half of 2019 levels throughout the second half of 2020. As a result, the cumulative reduction in 2020 emission due to international bunkers was 75% that of the reduction due to traffic, despite the comparatively small magnitude of the daily emissions from international bunkers.

Sustained reduction in other sectors will require investment in renewable energy and new technologies to support current levels of productivity with lower carbon emissions, that is, to reduce the carbon intensity of our economy. Such investment is essential, as several studies (54, 55) have documented the harm to employment, family connections, and other critical human connections from the reduction in personal mobility due to the pandemic. Liu et al. (13) note that Spain's 2020 emissions due to power generation were almost 25% lower than in 2019 due to investment in renewable energy. A post-COVID economic recovery represents an opportunity to invest in carbon-reducing technologies (56), as long as the need to balance short-term job creation with long-term retraining is accounted for (57). If this investment was able to continue the trend of a 5.4% decrease in global CO_2 emissions per year, we would reach "preindustrial" (circa 1850) emissions levels in approximately 18 years.

Strengths and weaknesses of current observing systems

Understanding how the COVID-19 pandemic has altered AQ and the carbon cycle has relied heavily on the multifaceted observing system built over the past two decades, including satellites, dense ground-based observing networks, Earth system and chemical transport models, and techniques to assimilate observations into these models. Novel data on human activity (particularly internet-of-things mobility data, crowdsourced air traffic data, and even news reports) have also played a vital role in both understanding how human behavior changed during the pandemic and quantifying the effect of that change on anthropogenic emissions.

Nevertheless, there remain important gaps in our observing network. First, space-based detection of VOCs remains a challenging problem, yet quantitative measurements of key biogenic (e.g. isoprene, terpenes) and anthropogenic (e.g. ethene, propene) contributors to VOC OH reactivity are needed to identify the dominant chemistry governing AQ around the globe. Second, as we saw in the LA Basin case study, disentangling primary PM emission, secondary PM formation, and meteorological drivers of PM concentration is crucial to understand which processes control PM exposure. Given the serious health impacts of PM exposure, work towards an integrated surface and space-based system that can differentiate these processes is needed to elucidate the optimum approaches to reducing PM exposure.

In regards to climate-relevant observations, spatiotemporally broader and denser space-based GHG observations would provide a highly valuable empirical constraint on changes to anthropogenic and biogenic carbon fluxes. A satellite instrument that provided comparable observations to the BEACO$_2$N network in the San Francisco Bay area ($\sim$ 2 km resolution, strong sensitivity to the near-surface atmosphere, urban-scale coverage) could apply similar inversion techniques as Turner et al. (16) to infer key sectors' emissions in cities around the world. It is also clear that our current network of near-real time ocean carbon uptake measurements are not sufficient to disentangle internal variability in the air-sea carbon flux from changes driven by reductions in anthropogenic emissions (25). Expanding this network or developing new methods to constrain the air-sea carbon flux from space will be necessary to quantify the impact of anthropogenic emissions reductions on atmospheric CO_2 mixing ratios.

Conclusions

The COVID-19 pandemic and associated changes in human behavior represent an unprecedented rapid change in anthropogenic emissions to the atmosphere. Due to the large differences in relevant atmospheric lifetimes for constituents central to AQ and climate, clear changes in local AQ but not global GHG trajectories were observed. Changes in AQ were very spatially heterogeneous, demonstrating that the same strategies to improve AQ do not apply equally well to all regions. Additionally, changes in AQ in the Los Angeles Basin correlated with temperature, precipitation, and severe wildfires, indicating that shifts in these quantities associated with climate change will at least partially offset gains in AQ made from past and future reductions in anthropogenic emissions.

Despite large disruptions in transportation emissions sectors, the global-scale change in the CO_2 growth rate was less than interannual variability. This is due to a combination of reduced ocean uptake of CO_2, a recovery of CO_2 emissions in the second half of 2020, and large interannual variability in land carbon fluxes. That recovery indicates that expecting changes to individual behavior to be sufficient to halt the increase of GHGs in the atmosphere is unrealistic. Instead, incentives to deploy new methods to systematically and sustainably reduce carbon intensity are needed. Given the bidirectional feedback between climate and AQ, it is clear that climate and AQ can no longer be considered separate problems; prompt action to reduce anthropogenic carbon emissions is essential not only to

avert direct climate impacts, but to avoid giving up decades of hard-won progress in improving urban AQ.

Materials and Methods

Full methods are available in the SI. Analysis of LA Basin AQ used data from CA Air Resources Board monitors, filtered for complete data records in the 2015 to 2020 period. 1 h daily maximum (DM) NO_2 and temperature, 8 h DM O_3, and 24 h average PM were calculated from this data. OPE was derived from model simulations using multiconstituent assimilation of multiple satellite measurements in the MIROC-CHASER model (32). OPE calculated by comparing modeled O_3 production and NO_x emission difference between baseline (2010 to 2019) and reduced 2020 emissions. Separate $PM_{2.5}$ simulations used GEOS-Chem v9-02 with NO_x emissions consistent with the OPE simulations: baseline NO_x emissions used HTAP v2 scaled to 2017 using satellite-derived emissions reduction ratios and COVID NO_x emissions were scaled down by the same factor as in the OPE simulations. The TROPOMI timeseries analysis first regridded native TROPOMI pixels to a $0.01° \times 0.01°$ grid and filtered to primarily remove cloud and snow/ice contaminated scenes. The timeseries show the 75th percentile of 15-day rolling average NO_2 columns in a $1° \times 1°$ box around each city.

Global CO_2 emissions estimates were derived from an array of near-real time data on power generation, industry, transport, and fuel consumption. XCO_2 growth rates were derived from OCO-2 v10 ocean glint data and XCH_4 growth rates from TCCON GGG2014 data. The data shown are 15-day running averages deseasonalized by fitting a four-harmonic curve. Expected CH_4 trends we computed from a two-box model (representing the two hemispheres) using prescribed OH concentrations and constant CH_4 emissions after 2012. TCCON data can be obtained from the TCCON Data Archive hosted by CaltechDATA (https://tccondata.org./). The authors thank the TCCON science team for their effort in providing this data.

Publicly available datasets are listed along with data generated from this study and stored in public facing repositories in the SI, table S1. Emissions data for Figs. 3 and 9 are given in Table S2. Data for the OPE values in Fig. 7 is given in Table S4. Emissions and OPE data also included as Excel SI files.

ACKNOWLEDGMENTS. The authors thank the Keck Institute for Space Studies for organizing and supporting the study "COVID-19: Identifying Unique Opportunities for Earth System Science" that led to the writing of this manuscript. The authors also acknowledge the use of data from the Port of Oakland and Port of LA website, Apple mobility data, and US EIA electricity use data. The authors also thank Charles Carter for his artwork in Figure 1. The views expressed in this manuscript are solely those of the authors and do not necessarily reflect those of the South Coast Air Quality Management District. A portion of this research was carried out at the Jet Propulsion Laboratory, California Institute of Technology, under contract with NASA. The authors acknowledge funding from the NASA and NSF: NASA grant NNX17AE15G (JL and PW), NASA CMS grant 80NSSC20K0006 (AC), NASA grant 80NSSC18K0689 (DH and HC), NASA Aura Science Team Program 19-AURAST19-0044 (KM and K. Bowman), NASA grant 80NSSC20K1122 (DG and SA), NSF RAPID grant 2030049 (K. Barsanti), NSF grants OCE-1752724 and OCE-1948664 (NL), and NSF grant OCE-1948624 (GM). AJT was supported as a Miller Fellow with the Miller Institute for Basic Research in Science at UC Berkeley. KG was supported by Northern Arizona University startup funds. CI was supported by University of California Institute of Transportation Studies. SS and ZZ were supported by California Air Resources Board, NASA Science Mission Directorate/Earth Science Division and JPL Earth Science and Technology Directorate. YLY was supported in part by the Jet Propulsion Laboratory OCO-2 grant JPL.1613918 to Caltech. JL would like to acknowledge funding support from NASA OCO science team program.

1. T Hale, et al., Oxford COVID-19 government response tracker. Blavatnik School of Government. (2020).
2. M Strohmeier, X Olive, J Lübbe, M Schäfer, V Lenders, Crowdsourced air traffic data from the OpenSky network 2019–20. *Earth Syst. Sci. Data Discuss.* **2020**, 1–15 (2020).
3. M Schäfer, M Strohmeier, V Lenders, I Martinovic, M Wilhelm, Bringing Up OpenSky: A Large-scale ADS-B Sensor Network for Research. *Proceedings of the 13th IEEE/ACM International Symposium on Information Processing in Sensor Networks (IPSN)*, 83–94 (2014).
4. X Olive, traffic, a toolbox for processing and analysing air traffic data. *J. Open Source Softw.* **4** (2019).
5. C Lamprecht, M Graus, M Striednig, M Stichaner, T Karl, Decoupling of urban CO_2 and air pollutant emission reductions during the european SARS-CoV-2 lockdown. *Atmospheric Chem. Phys.* **21**, 3091–3102 (2021).
6. DL Goldberg, et al., Disentangling the impact of the COVID-19 lockdowns on urban NO_2 from natural variability. *Geophys. Res. Lett.* **47** (2020).
7. K Miyazaki, et al., Global tropospheric ozone responses to reduced NO_x emissions linked to the COVID-19 world-wide lockdowns. *Sci. Adv.* **7**, eabf7460 (2021).
8. CA Keller, et al., Global impact of covid-19 restrictions on the surface concentrations of nitrogen dioxide and ozone. *Atmospheric Chem. Phys.* **21**, 3555–3592 (2021).
9. J Xing, et al., Quantifying the emission changes and associated air quality impacts during the COVID-19 pandemic on the north china plain: a response modeling study. *Atmospheric Chem. Phys.* **20**, 14347–14359 (2020).
10. M Guevara, et al., Time-resolved emission reductions for atmospheric chemistry modelling in europe during the COVID-19 lockdowns. *Atmospheric Chem. Phys.* **21**, 773–797 (2021).
11. T Doumbia, et al., Changes in global air pollutant emissions during the COVID-19 pandemic: a dataset for atmospheric chemistry modeling. *Earth Syst. Sci. Data* (2021).
12. International Energy Agency, Methane tracker 2021 (https://www.iea.org/reports/methane-tracker-2021) (2021) last accessed 22 Apr 2021.
13. Z Liu, et al., Global daily CO_2 emissions for the year 2020 (2021).
14. C Le Quéré, et al., Temporary reduction in daily global CO_2 emissions during the COVID-19 forced confinement. *Nat. Clim. Chang.* **10**, 647–653 (2020).
15. Z Liu, et al., Near-real-time monitoring of global CO_2 emissions reveals the effects of the COVID-19 pandemic (2020).
16. AJ Turner, et al., Observed impacts of COVID-19 on urban CO_2 emissions. *Geophys. Res. Lett.* **47**, e2020GL090037 (2020).
17. D Liu, et al., Observed decreases in on-road co_2 concentrations in beijing during covid-19. *Atmospheric Chem. Phys. Discuss.* **2020**, 1–18 (2020).
18. M Buchwitz, et al., Can a regional-scale reduction of atmospheric co_2 during the covid-19 pandemic be detected from space? a case study for east china using satellite xco_2 retrievals. *Atmospheric Meas. Tech.* **14**, 2141–2166 (2021).
19. RM Duren, et al., California's methane super-emitters. *Nature* **575**, 180–184 (2019).
20. BK Lamb, et al., Direct measurements show decreasing methane emissions from natural gas local distribution systems in the united states. *Environ. Sci. & Technol.* **49**, 5161–5169 (2015).
21. DR Lyon, et al., Concurrent variation in oil and gas methane emissions and oil price during the COVID-19 pandemic. *Atmospheric Chem. Phys.* **21**, 6605–6626 (2021).
22. National Oceanic and Atmospheric Administration, Annual mean global carbon dioxide growth rates (https://www.esrl.noaa.gov/gmd/ccgg/trends/gl_gr.html) (2021) last accessed 26 Apr 2021.
23. T Shiraishi, R Hirata, Estimation of carbon dioxide emissions from the megafires of australia in 2019–2020. *Sci. Reports* **11** (2021).
24. JC Fyfe, et al., Quantifying the influence of short-term emission reductions on climate. *Sci. Adv.* **7** (2021).
25. NS Lovenduski, et al., The ocean carbon response to COVID-related emissions reductions. *Geophys. Res. Lett.* **48** (2021).
26. D Wunch, et al., The Total Carbon Column Observing Network. *Philos. Transactions Royal Soc. A: Math. Phys. Eng. Sci.* **369**, 2087–2112 (2011).
27. D Wunch, et al., The Total Carbon Column Observing Network's GGG2014 data version, Technical report (2015).
28. PO Wennberg, et al., TCCON data from Park Falls (US), Release GGG2014R0 (TCCON data archive, hosted by CaltechDATA) (2014).
29. V Sherlock, et al., TCCON data from Lauder (NZ), 125HR, Release GGG2014R0 (TCCON data archive, hosted by CaltechDATA) (2014).
30. DF Pollard, J Robinson, H Shiona, TCCON data from Lauder (NZ), Release GGG2014.R0 (TCCON data archive, hosted by CaltechDATA) (2019).
31. National Oceanic and Atmospheric Administration, Despite pandemic shutdowns, carbon dioxide and methane surged in 2020 (https://research.noaa.gov/article/ArtMID/587/ArticleID/2742/Despite-pandemic-shutdowns-carbon-dioxide-and-methane-surged-in-2020) (2021) last accessed 26 Apr 2021.
32. K Miyazaki, et al., Updated tropospheric chemistry reanalysis and emission estimates, TCR-2, for 2005–2018. *Earth Syst. Sci. Data* **12**, 2223–2259 (2020).
33. AJ Turner, C Frankenberg, EA Kort, Interpreting contemporary trends in atmospheric methane. *Proc. Natl. Acad. Sci.* **116**, 2805–2813 (2019).
34. Y Zhao, et al., Substantial changes in nitrogen dioxide and ozone after excluding meteorological impacts during the COVID-19 outbreak in mainland china. *Environ. Sci. Technol. Lett.* **7**, 402–408 (2020).
35. SK Grange, et al., Covid-19 lockdowns highlight a risk of increasing ozone pollution in european urban areas. *Atmospheric Chem. Phys.* **21**, 4169–4185 (2021).
36. JD Lee, WS Drysdale, DP Finch, SE Wilde, PI Palmer, UK surface NO_2 levels dropped by 42 % during the COVID-19 lockdown: impact on surface O_3. *Atmospheric Chem. Phys.* **20**, 15743–15759 (2020).
37. P Messina, et al., Global biogenic volatile organic compound emissions in the ORCHIDEE and MEGAN models and sensitivity to key parameters. *Atmospheric Chem. Phys.* **16**, 14169–14202 (2016).
38. HA Parker, S Hasheminassab, JD Crounse, CM Roehl, PO Wennberg, Impacts of traffic reductions associated with COVID-19 on Southern California air quality. *Geophys. Res. Lett.* **47** (2020).
39. C Ivey, et al., Impacts of the 2020 COVID-19 Shutdown Measures on Ozone Production in the Los Angeles Basin, preprint (2020).
40. DJ Rasmussen, J Hu, A Mahmud, MJ Kleeman, The ozone–climate penalty: Past, present,

and future. *Environ. Sci. & Technol.* **47**, 14258–14266 (2013).
41. U.S. EPA, Integrated science assessment (ISA) for particulate matter, (U.S. Environmental Protection Agency, Washington, D.C.), Technical Report EPA/600/R-19/188 (2019).
42. AS Ansari, SN Pandis, Response of inorganic PM to precursor concentrations. *Environ. Sci. & Technol.* **32**, 2706–2714 (1998).
43. MS Hammer, et al., Effects of COVID-19 lockdowns on fine particular matter concentrations. *Sci. Adv.* (in press).
44. JD Berman, K Ebisu, Changes in U.S. air pollution during the COVID-19 pandemic. *Sci. The Total. Environ.* **739**, 139864 (2020).
45. Z Zheng, G Xu, Q Li, C Chen, J Li, Effect of precipitation on reducing atmospheric pollutant over Beijing. *Atmospheric Pollut. Res.* **10**, 1443–1453 (2019).
46. X Zhao, Y Sun, C Zhao, H Jiang, Impact of precipitation with different intensity on PM2.5 over typical regions of China. *Atmosphere* **11**, 906 (2020).
47. Z Jiang, et al., Unexpected slowdown of US pollutant emission reduction in the past decade. *Proc. Natl. Acad. Sci.* **115**, 5099–5104 (2018).
48. JL Laughner, RC Cohen, Direct observation of changing NO_x lifetime in North American cities. *Science* **366**, 723–727 (2019).
49. DT Shindell, Y Lee, G Faluvegi, Climate and health impacts of US emissions reductions consistent with 2 °C. *Nat. Clim. Chang.* **6**, 503–507 (2016).
50. SE Pusede, AL Steiner, RC Cohen, Temperature and recent trends in the chemistry of continental surface ozone. *Chem. Rev.* **115**, 3898–3918 (2015).
51. AP Williams, et al., Observed impacts of anthropogenic climate change on wildfire in california. *Earth's Futur.* **7**, 892–910 (2019).
52. T Stocker, et al., Technical summary in *Climate Change 2013: The Physical Science Basis. Contribution of Working Group I to the Fifth Assessment Report of the Intergovernmental Panel on Climate Change*, eds. T Stocker, et al. (Cambridge University Press, Cambridge, United Kingdom and New York, NY, USA), (2013).
53. S Ridge, G McKinley, Ocean carbon uptake under aggressive emission mitigation. *Biogeosciences* **18**, 2711–2725 (2021).
54. L Brubaker, Women physicians and the COVID-19 pandemic. *JAMA* **324**, 835 (2020).
55. JLC Kok, Short-term trade-off between stringency and economic growth. *COVID Econ.* **60**, 172–189 (2020).
56. EB Barbier, Greening the post-pandemic recovery in the G20. *Environ. Resour. Econ.* **76**, 685–703 (2020).
57. Z Chen, G Marin, D Popp, F Vona, Green stimulus in a post-pandemic recovery: the role of skills for a resilient recovery. *Environ. Resour. Econ.* **76**, 901–911 (2020).

PNAS
www.pnas.org

Supplementary Information for

Societal shifts due to COVID-19 reveal large-scale complexities and feedbacks between atmospheric chemistry and climate change

Joshua L. Laughner, Jessica L. Neu, David Schimel, Paul O. Wennberg, et al.

Full author list:
Joshua L. Laughner, Jessica L. Neu, David Schimel, Paul O. Wennberg, Kelley Barsanti, Kevin Bowman, Abhishek Chatterjee, Bart Croes, Helen Fitzmaurice, Daven Henze, Jinsol Kim, Eric A. Kort, Zhu Liu, Kazuyuki Miyazaki, Alexander J. Turner, Susan Anenberg, Jeremy Avise, Hansen Cao, David Crisp, Joost de Gouw, Annmarie Eldering, John Fyfe, Dan Goldberg, Kevin R. Gurney, Sina Hasheminassab, Francesca Hopkins, Cesunica E. Ivey, Dylan B.A. Jones, Junjie Liu, Nicole S. Lovenduski, Randall V. Martin, Galen A. McKinley, Lesley Ott, Benjamin Poulter, Muye Ru, Stanley P. Sander, Neil Swart, Yuk L. Yung, Zhao-Cheng Zeng, and the rest of the Keck Institute for Space Studies "COVID-19: Identifying Unique Opportunities for Earth System Science" study team

Corresponding Authors:
Joshua L. Laughner: jlaugh@caltech.edu
Jessica L. Neu: jessica.l.neu@jpl.nasa.gov
David Schimel: david.schimel@jpl.nasa.gov, or
Paul O. Wennberg: wennberg@gps.caltech.edu

This PDF file includes:

Supplementary text
Figs. S1 to S11
Tables S1 to S4
References for SI reference citations

Study team author list

The Keck Institute for Space Studies "COVID-19: Identifying Unique Opportunities for Earth System Science" study team includes the following members in addition to the named authors:

- Ron Cohen: University of California Berkeley
- Dan Crichton: Jet Propulsion Laboratory
- John Crounse: California Institute of Technology
- Dan Cusworth: Jet Propulsion Laboratory
- Kevin Donkers: Met Office Informatics Lab (UK)
- Zac Flamig: Amazon
- Joe Flasher: Amazon
- Christian Frankenberg: California Institute of Technology
- Meredith Franklin: University of Southern California
- Randy Friedl: Jet Propulsion Laboratory
- Michael Garay: Jet Propulsion Laboratory
- Chelle Gentemann: Farallon Institute
- Shane Glass: Google
- Kathy Hibbard: National Aeronautics and Space Administration
- Glynn Hulley: Jet Propulsion Laboratory
- Ken Jucks: National Aeronautics and Space Administration
- Olga Kalashnikova: Jet Propulsion Laboratory
- Emma Knowland: National Aeronautics and Space Administration/Goddard Space Flight Center
- Jean-Francois Lamarque: National Center for Atmospheric Research
- Barry Lefer: National Aeronautics and Space Administration
- Chip Miller: Jet Propulsion Laboratory
- Pami Mukherjee: South Coast Air Quality Management District
- Olga Pikelnaya: South Coast Air Quality Management District
- Tom Prince: Keck Institute for Space Studies
- Chris Ruf: Univ. of Michigan
- Natasha Stavros: Jet Propulsion Laboratory
- Britt Stephens: National Center for Atmospheric Research
- Colm Sweeney: National Oceanic and Atmospheric Administration
- Andrew Thorpe: Jet Propulsion Laboratory
- Karin Tuxen-Bettman: Google
- Duane Waliser: Jet Propulsion Laboratory
- Yuan Wang: California Institute of Technology
- Helen Worden: National Center for Atmospheric Research
- Yuqiang Zhang: Duke University

Additional figures

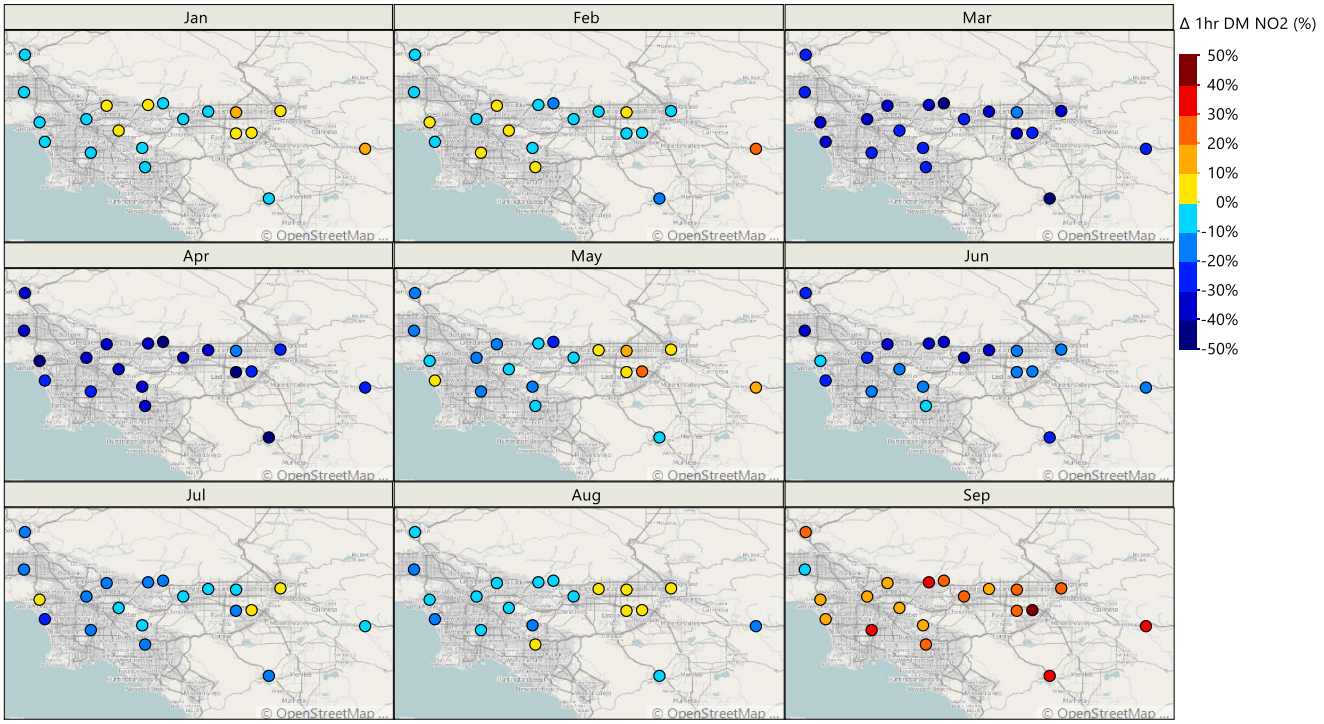

Fig. S1. Change in 1 hr daily maximum (DM) NO_2 in 2020 relative to the average of 2015 to 2019 at the California Air Resources Board sites throughout the South Coast Air Basin.

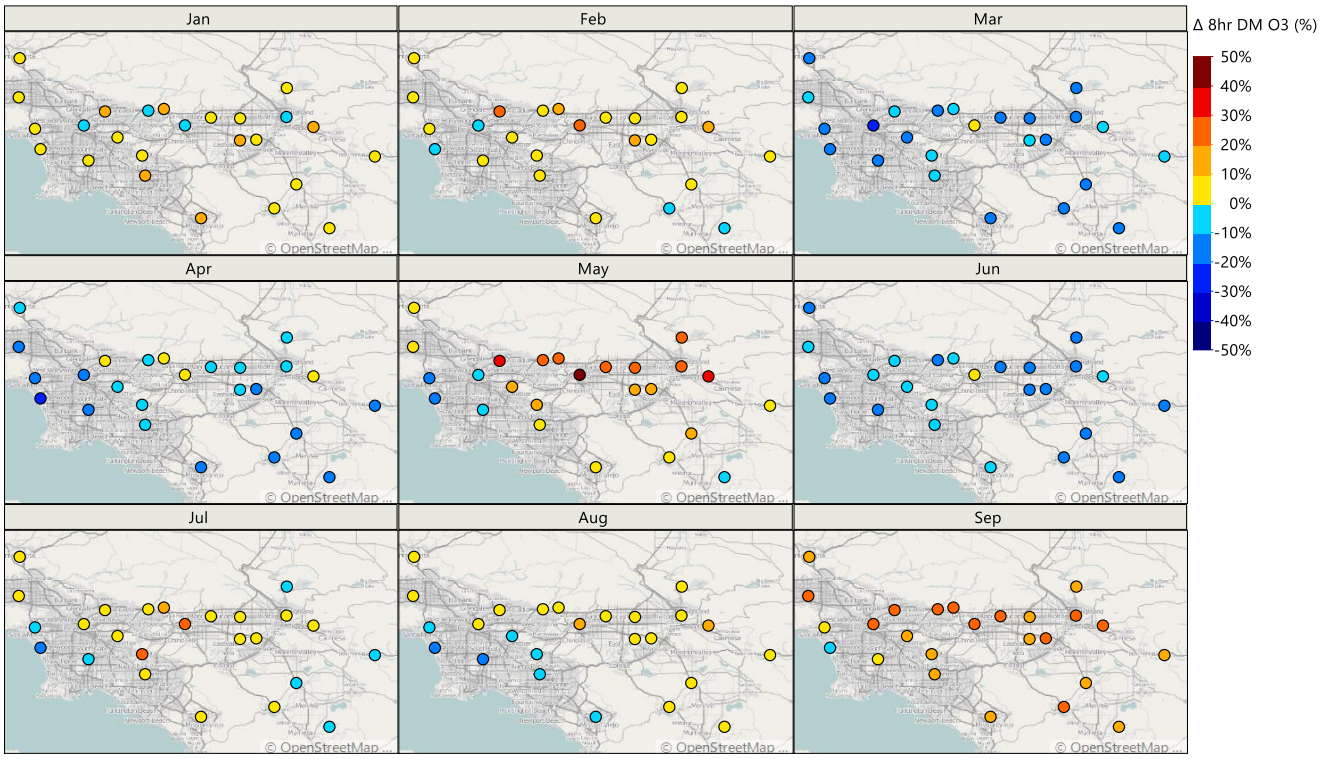

Fig. S2. Change in 8 hr daily maximum (DM) O_3 in 2020 relative to the average of 2015 to 2019 at the California Air Resources Board sites throughout the South Coast Air Basin.

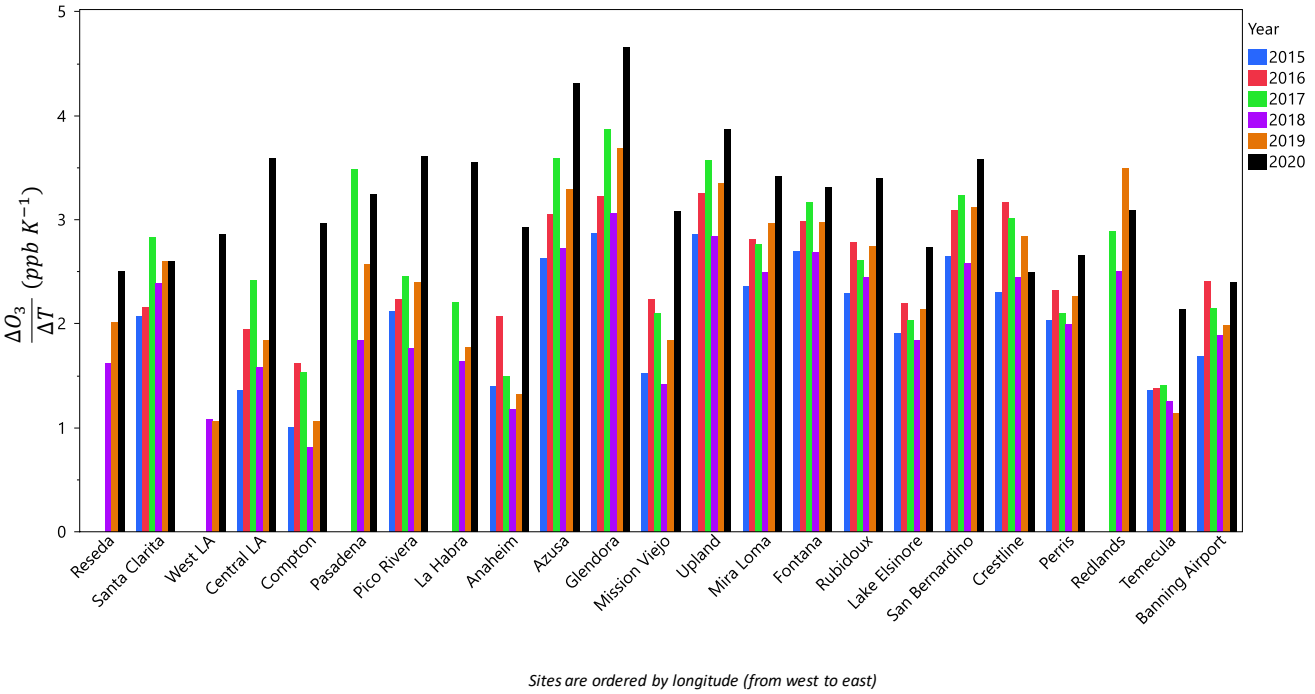

Fig. S3. Average derivatives of O_3 response vs. temperature between May and September at California Air Resources Board sites throughout the South Cost Air Basin for years 2015–2020. Each group of bars is one site, and are ordered by longitude (west to east).

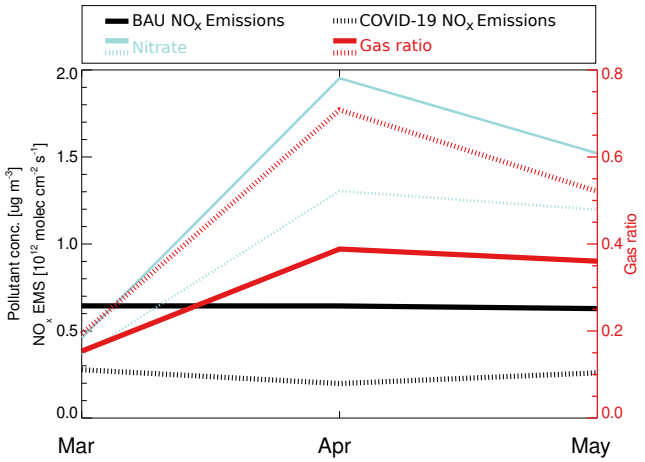

Fig. S4. Simulated inorganic nitrate aerosol sensitivity at downtown LA for two model runs during March to May 2020. Dashed lines represent the run with lockdown-induced emissions reductions (COVID-19), solid lines represent the business as usual (BAU) run. NO_x emissions are shown in black, nitrate aerosol concentration in blue, and the gas ratio in red. A gas ratio < 1 indicates NH_3-limited (compared to NO_x-limited chemistry). See the SI for more information.

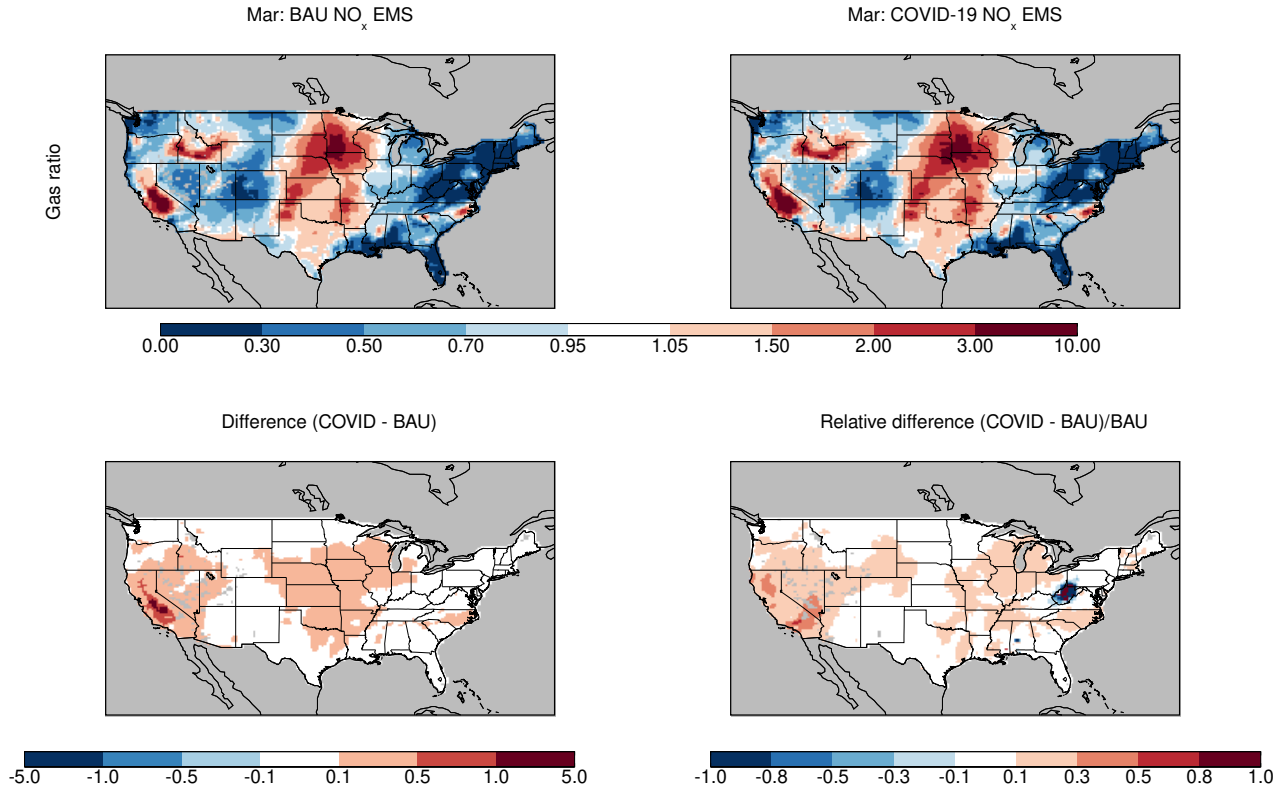

Fig. S5. Average change in gas ratios for March 2020 between a model simulation using business as usual (BAU) NO_x emissions and one using emissions based on NO_2 observations for March 2020 (COVID-19). The gas ratio is described in Eq. (3); a value < 1 indicates NH_3 limited nitrate aerosol formation; a value > 1 indicates NO_x limited aerosol formation.

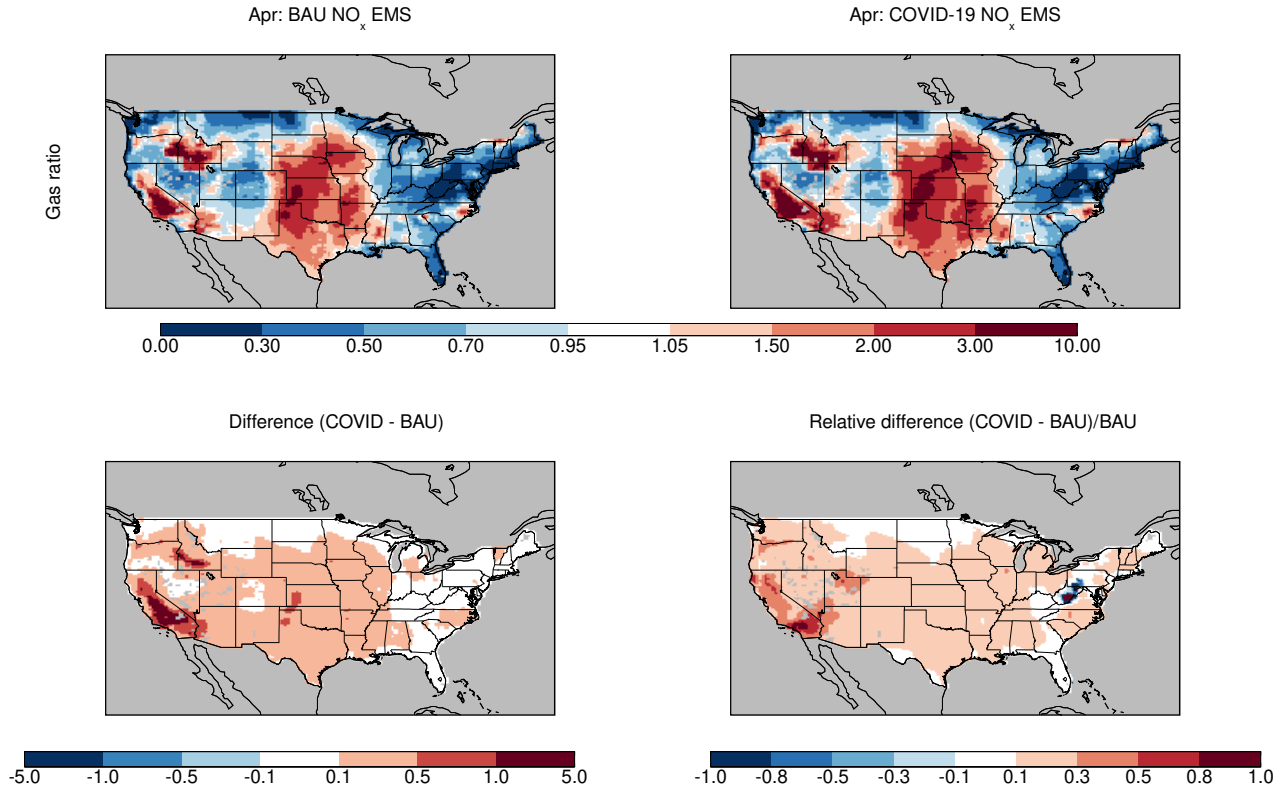

Fig. S6. Same as Fig. S7, but for April 2020.

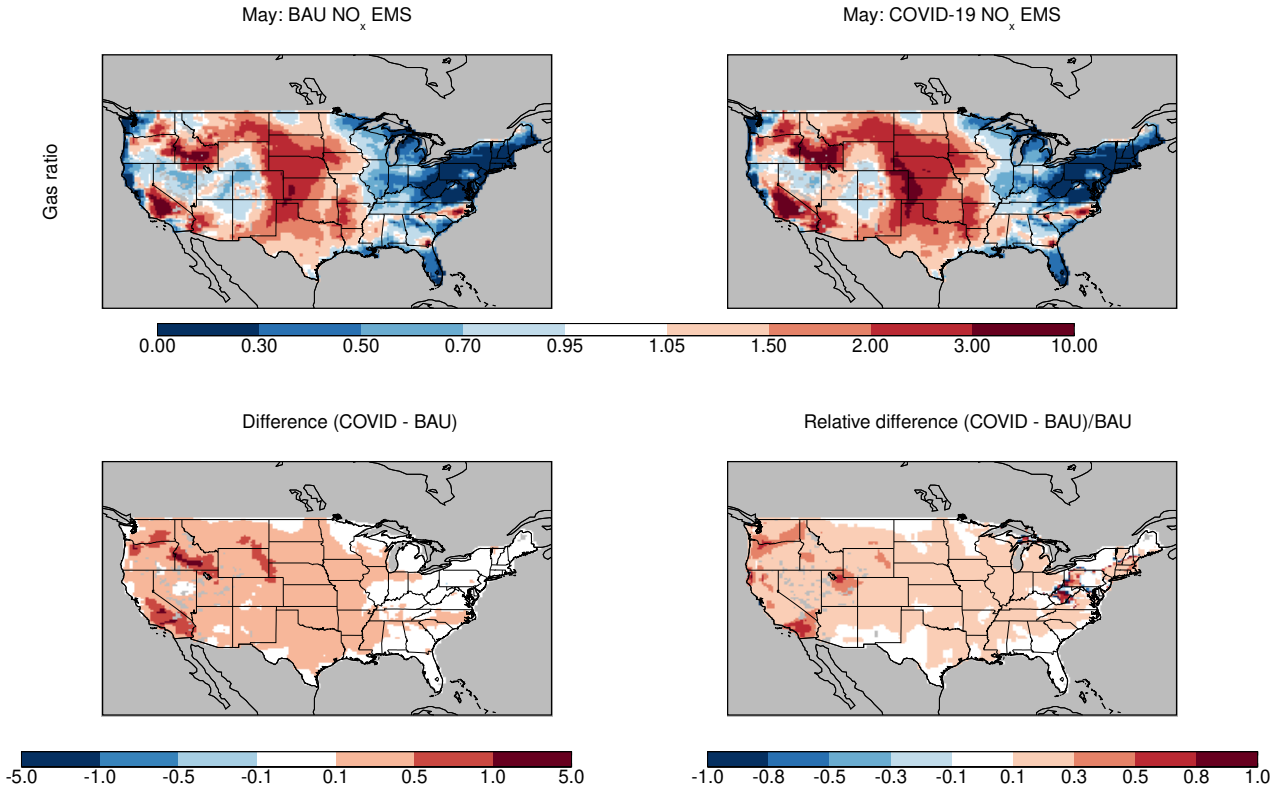

Fig. S7. Same as Fig. S7, but for May 2020.

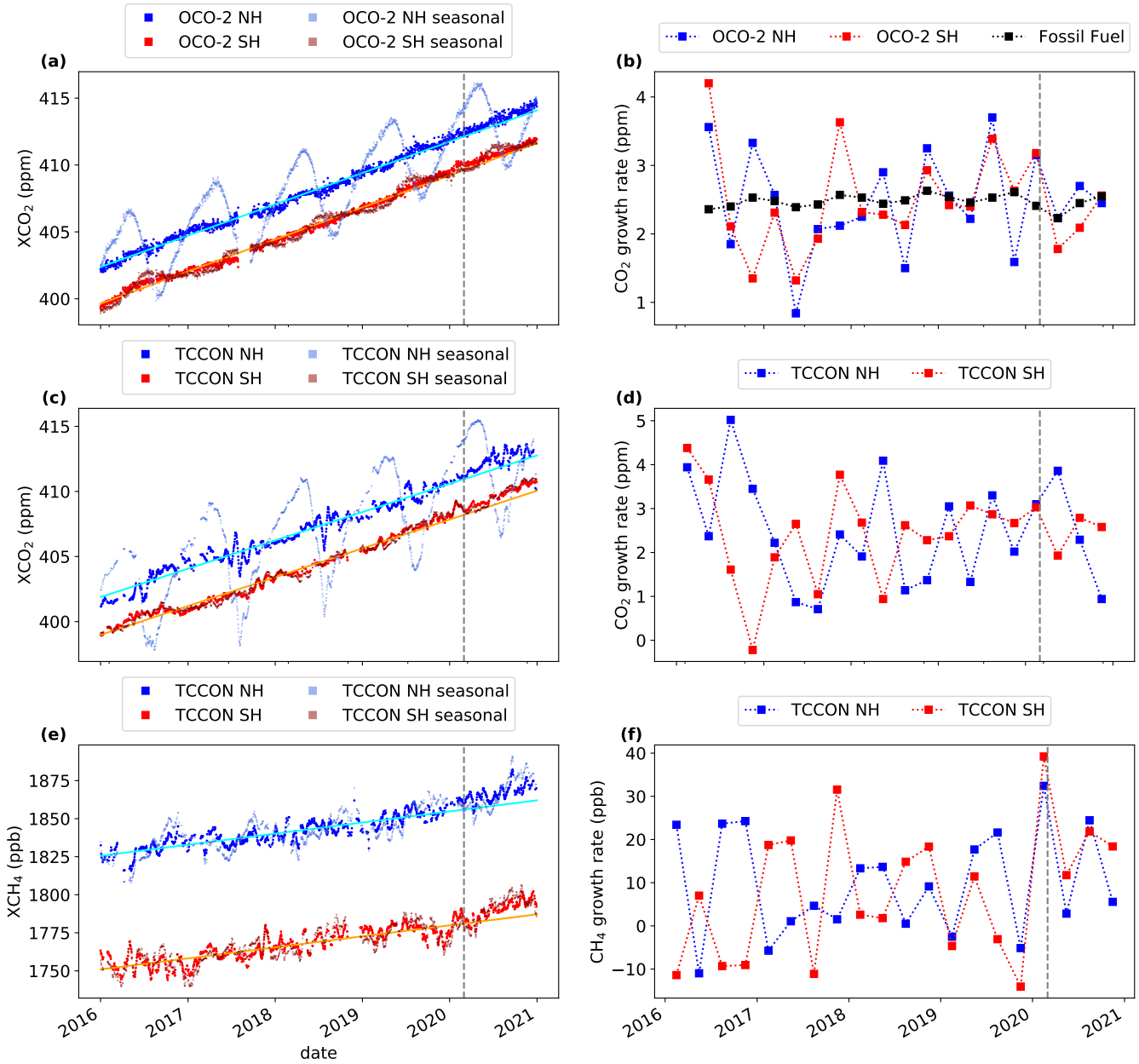

Fig. S8. Trends in column average CO_2 and CH_4. **(a)** Trends in CO_2 from the Orbiting Carbon Observatory 2 (OCO-2) for the northern and southern hemispheres. The pale blue and red markers are daily values, calculated as described in the text. The vibrant blue and red markers represent deseasonalized values computed from the daily values by fitting a fixed seasonal cycle described by a four-term harmonic equation (1, 2). The solid line is a robust linear fit to the 2016 through 2019 data. **(b)** Annual growth rate of CO_2 computed from OCO-2 data in the northern and southern hemispheres, as well as derived from fossil fuel emissions trends. See text for details. **(c)** As (a), but for CO_2 from two Total Carbon Column Observing Network (TCCON) stations: Park Falls, WI, USA in the northen hemisphere and Lauder, New Zealand in the southern hemisphere. **(d)** As (b), but derived from TCCON CO_2. **(e)** As (c), but for CH_4. **(f)** As (d), but for CH_4. In all panels the vertical gray dashed line marks 1 March 2020.

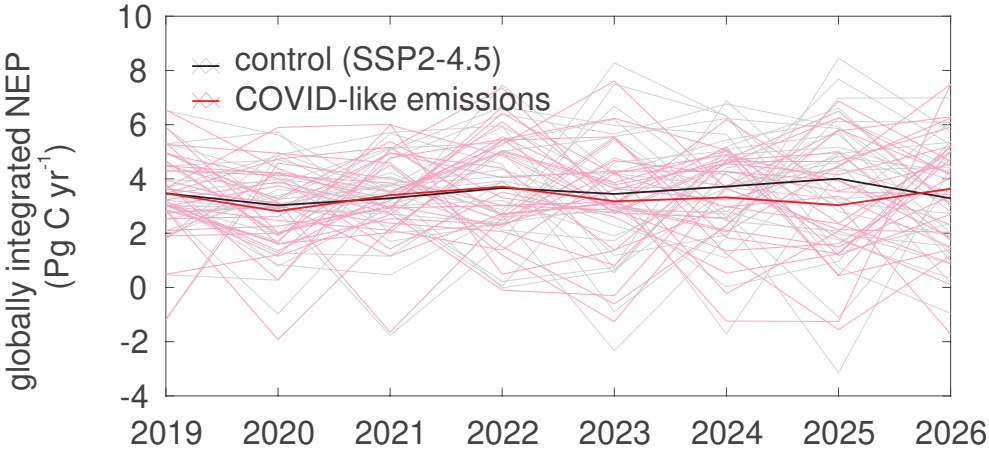

Fig. S9. Annual mean, globally integrated terrestrial net ecosystem production (NEP, positive into biosphere, excludes land use change) predicted from the CanESM5-COVID ensemble (3). As in the main paper, black/gray lines derive from simulations forced with SSP2-RCP4.5 CO_2 emissions, while red/pink lines derive from simulations forced with a 25% peak CO_2 emissions reduction in 2020. See (3) for more details. Thick lines are ensemble averages, and thin lines are individual ensemble members, each with different phasing of internal variability.

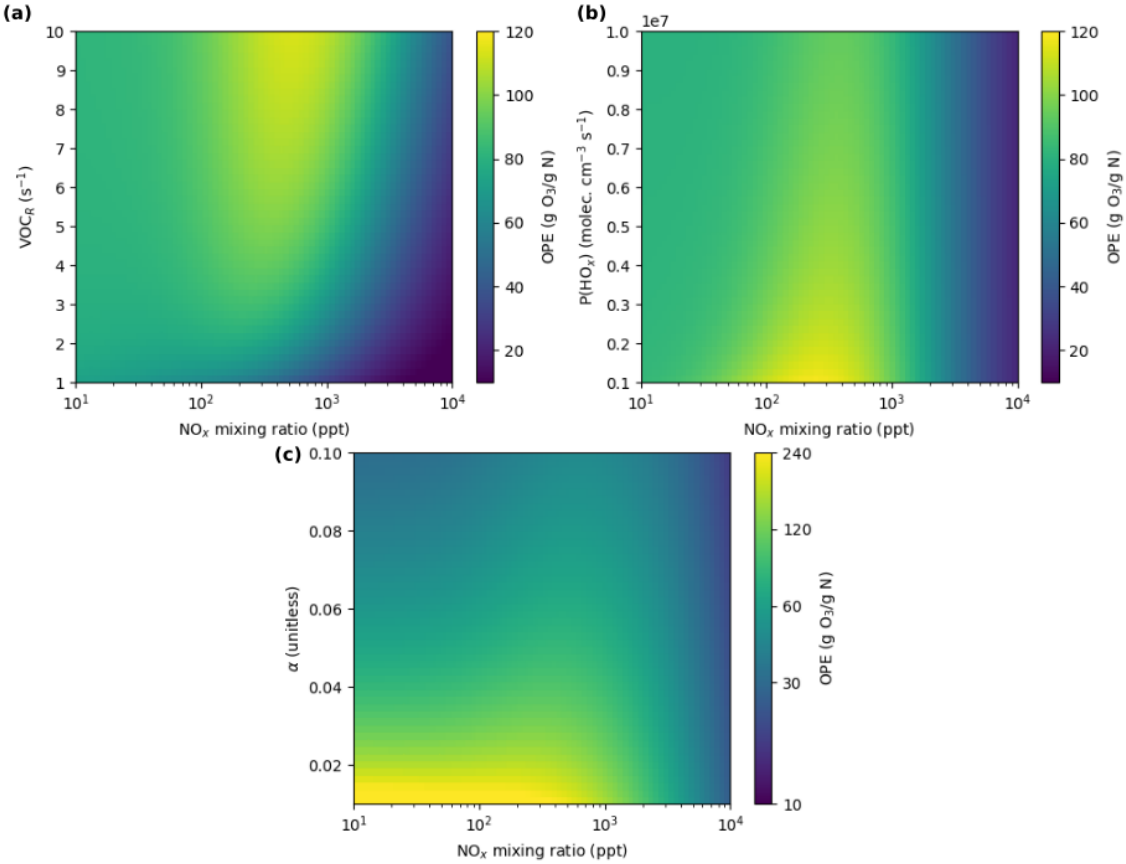

Fig. S10. Theoretical ozone production efficiency as a function of NO_x concentration and one other variable, computed in a steady-state model. In all panels, NO_x concentration is given on the x-axis, the second independent variable on the y-axis, and the color represents the ozone production efficiency. In panel **(a)**, the y-axis is total VOC reactivity, VOC_R; in panel **(b)**, it is total HO_x production, P(HO_x); in panel **(c)**, it is the branching ratio (α) for the RO_2 + NO reaction. Note that the y-axis in panel (b) is multiplied by 10^7 and the color scale for panel (c) has a higher maximum value than the other panels and is logarithmic, rather than linear. The default values for VOC_R, P(HO_x), and α when not the second dependent variables are 5.0 s^{-1}, 6.25×10^6 molec. cm^{-3} s^{-1}, and 0.04, respectively.

Supporting Information Text

Methods

Public data. All public datasets used in this study are shown in Table S1.

Human activity metrics. The human activity metrics in Fig. 2 include the Oxford Coronavirus Government Response Index (4), Opensky-derived flight data (5, 24, 25), Port of LA container moves (https://www.portoflosangeles.org/business/statistics/container-statistics, last accessed 13 May 2021), Port of Long Beach container moves (https://www.polb.com/business/port-statistics/#teus-archive-1995-to-present, last access 20 Feb 2021) Port of Oakland container moves (https://www.oaklandseaport.com/performance/facts-figures/, last accessed 13 May 2021), Caltrans PeMS daily vehicle counts (http://pems.dot.ca.gov/, last accessed 30 Mar 2021), Apple driving mobility data (https://covid19.apple.com/mobility, last accessed 20 Feb 2021), and U.S. Energy Information Agency electricity consumption (https://www.eia.gov/electricity/data/browser/#/topic/, last accessed 20 Feb 2021).

The CAADA Python package (26) was used to preprocess the PeMS vehicle counts and Strohmeier et al. (5) flight data, as well as download Port of LA and Port of Oakland container moves. For the purposes of Fig. 2, "Bay Area" is defined as Alameda, Contra Costa, Marin, San Mateo, San Francisco, Santa Clara, and Santa Cruz counties, while "LA" is defined as Los Angeles, Orange, Riverside, San Bernardino, Santa Barbara, and Ventura counties. For flight data, shipping data, and traffic data, daily values were normalized such that 15 Jan 2020 is 100% and monthly values were normalized such that Jan 2020 was 100%. For electricity use data, each month's value is the 2020 use as a percentage of 2019 use in the same month.

Oxford stringency index: US vs. US state mean. The Oxford Stringency Index (27) includes stringency metrics labeled as US without a subregional code along with metrics for individual states. In Fig. 2, "United States" indicates that the US values without a subregional code are plotted, while "US (state mean)" indicates that the average of all the individual states' stringency indices is plotted. The Oxford index subnational interpretation guide (https://github.com/OxCGRT/covid-policy-tracker/blob/master/documentation/subnational_interpretation.md, last accessed 13 May 2021) indicates that their primary dataset summarizes the totality of policies in the specified territory.

While we include both the combined US and state mean metric to illustrate the general stringency of lockdown measures in the US, we do not ascribe specific meaning to the difference between them.

Equivalent Emissions Year Calculations. For the CO_2 emissions in Fig.3, we used 2005-2018 fossil fuel emissions from the Global Carbon Budget 2019 (28). For 2019, we assumed a +0.1% increase from 2018 based on Supplementary Data in Le Quere et al (29). For 2020 we used a 7% decrease from the 2019 value with a $\pm$ 1% uncertainty, based on Le Quere et al (29) and Liu et al (30). The 2020 emissions are 9.29 ($\pm$ 0.10) GtC/yr; this corresponds to somewhere between 2010 (9.05 GtC/yr) and 2012 (9.50 GtC/yr). For CH_4, we use the anthropogenic emissions based on the EDGARv4.3.2 and GFED4.1s emissions inventories as published in the Global Methane Budget 2000-2017 (31). To estimate the emissions trajectory beyond 2017, we assumed that the rate of increase for 2018 and 2019 was equal to the average rate for 2005 to 2017, then used the estimated 10% reduction in 2020 from (32). For the global NO_x emission trajectory in Fig. 3 we used 2005-2020 emissions from the assimilation system described in the subsection "Global ozone production efficiency calculation" below.

For Fig 9, we again used the NO_x emissions from the assimilation system. For countries whose emissions have been monotonically increasing since 2005, we calculate the prior year with the same emissions as 2020. For countries whose emissions decreased over all or part of the 2005-2019 period, we use the 2015-2019 rate of decline to project emissions into the future.

Global CO_2 emissions estimates. We calculated the daily global fossil CO_2 emissions in 2020 (updated to December 31st), as well as the daily sectoral emissions from power sector, industry sector, transport sector (including ground transport, aviation and shipping), and residential sector respectively. The estimates are based on a set of near real time dataset including hourly to daily electrical power generation data from national electricity operation systems of 31 countries, real-time mobility data (TomTom city congestion index data of 416 cities worldwide and FlightRadar24 individual flight location data), monthly industrial production data (calculated separately by cement production, steel production, chemical production and other industrial production of 27 industries) or indices (primarily Industrial Production Index) from national statistics of 62 countries/regions, and monthly fuel consumption data corrected for the daily population-weighted air temperature in 206 countries.

CO_2 and CH_4 trends and CH_4 box model. CO_2 and CH_4 trends were computed from version 10 column average CO_2 (termed XCO_2) measurements made by the Orbiting Carbon Observatory 2 (OCO-2) satellite instrument and ground based CO_2 and CH_4 column measurements from two Total Carbon Column Observing Network (TCCON) sites: one in Park Falls, WI, USA (45.945° N, 90.273° W) and Lauder, New Zealand (45.038° S, 169.684° E). OCO-2 data was subset to quality flag = 0 data collected in the ocean glint mode and all data averaged daily between 20° N and 55° N for the northern hemisphere and 55° S and 20° S for the southern hemisphere. TCCON data was limited to data with flag = 0; publicly available data is already filtered in this manner.

To compute the trends, 15 day running averages of the daily data were computed and deseasonalized using the method in Liu et al. (1) which follows Graven et al. (2). A robust linear fit was applied to the 2016 through 2019 data. 2020 was excluded so as to test how the 2020 trend compared to the previous four years.

Growth rates were computed from the deseasonalized data by taking the differences in time of three month averages of the OCO-2 or TCCON deseasonalized data, multiplied by four to convert from three-monthly to annual growth rates. The growth

Dataset	Used for	Link	Last access	Citation
Oxford Stringency Index	Human activity metrics	https://www.bsg.ox.ac.uk/research/research-projects/coronavirus-government-response-tracker	20 Feb 2021	(4)
OpenSky-derived flight data	Human activity metrics	https://zenodo.org/record/3928564	31 Mar 2021	(5)
Port of Oakland container moves	Human activity metrics	https://www.oaklandseaport.com/performance/facts-figures/	13 May 2021	
Port of LA container moves	Human activity metrics	https://www.portoflosangeles.org/business/statistics/container-statistics	13 May 2021	
Port of Long Beach container moves	Human activity metrics	https://www.polb.com/business/port-statistics/#teus-archive-1995-to-present	20 Feb 2021	
Caltrans PeMS	Human activity & SF emissions	https://pems.dot.ca.gov/	30 Mar 2021	
Apple mobility trends	Human activity metrics	https://covid19.apple.com/mobility	20 Feb 2021	
US EIA electricity use	Human activity metrics	https://www.eia.gov/electricity/data/browser/#/topic/	20 Feb 2021	
CARB air quality data	LA Basin analysis	https://www.arb.ca.gov/aqmis2/aqdselect.php	11 Nov 2020	
OMI NO_2 columns	Global model assimilation (OPE)	http://www.qa4ecv.eu/ecv/no2-pre/data	11 Nov 2020	(6, 7)
TROPOMI NO_2 columns	Global model assimilation (OPE)	http://www.tropomi.eu/data-products/nitrogen-dioxide	11 Nov 2020	(8)
MOPITT CO	Global model assimilation (OPE)	https://www2.acom.ucar.edu/mopitt	11 Nov 2020	(9)
OMI SO_2 columns	Global model assimilation (OPE)	https://disc.gsfc.nasa.gov/datasets/OMSO2_003/summary	11 Nov 2020	(10, 11)
MLS O_3	Global model assimilation (OPE)	https://mls.jpl.nasa.gov/products/o3_product.php	11 Nov 2020	(12, 13)
MLS HNO_3	Global model assimilation (OPE)	https://mls.jpl.nasa.gov/products/hno3_product.php	11 Nov 2020	(12, 14)
BEACO2N CO_2 data	SF CO_2 emissions estimates	https://beacon.berkeley.edu/	11 Nov 2020	
OCO-2 XCO_2 V10	CO_2 trends	https://ocov2.jpl.nasa.gov/oco-2-data-center/	2 Apr 2021	(15–17)
TCCON CO_2 and CH_4 GGG2014 data	CO_2 & CH_4 trends	https://tccondata.org/	2 Apr 2021	(18–21)
ODIAC	2016–2019 CO_2 emissions for FF growth rate	https://www.odiac.org/index.html	2 Apr 2021	(22)
Carbon Monitor	2020 CO_2 emissions for FF growth rate and 2019/2020 emissions comparison	https://carbonmonitor.org/	2 Apr 2021	(23)
NOAA HRRR meteorology	SF CO_2 emissions estimates	https://rapidrefresh.noaa.gov/hrrr/	11 Nov 2020	
Ocean/land ensemble data	Ocean and land flux responses	http://crd-data-donnees-rdc.ec.gc.ca/CCCMA/publications/COVID19/.	27 May 2021	(3)
GEOS-Chem nitrate simulation	Response of nitrate PM2.5 to NO_x reductions	https://doi.org/10.5281/zenodo.4849416	29 May 2021	

Table S1. Public data sources used in this paper. The "Used for" column gives the part of the analysis in which that data was used.

Year	CO_2 (Gt C/yr)	CH_4 (Tg CH_4/yr)	NO_x (Tg N/yr)
2005	8.02	330.458	36.50
2006	8.29	341.481	37.02
2007	8.54	339.064	36.41
2008	8.73	341.426	36.47
2009	8.61	345.293	34.41
2010	9.05	352.484	36.16
2011	9.35	356.701	36.65
2012	9.50	363.326	35.75
2013	9.54	361.773	35.99
2014	9.61	369.790	37.04
2015	9.62	377.163	35.36
2016	9.66	371.620	33.77
2017	9.77	373.658	34.31
2018	9.98	-	34.30
2019	9.99	-	33.34
2020	9.29	-	30.58

Table S2. Emissions used in Figs. 3 and 9. A dash indicates that emissions data were not available for that year.

rate for fossil fuel emissions was computed by using three month total of anthropogenic CO_2 emissions from the Open-source Data Inventory for Anthropogenic CO_2 (ODIAC) for 2016 through 2019 and carbonmonitor.org for 2020. The three month total emitted CO_2 mass was converted to an atmospheric mixing ratio by:

$$R_{\mathrm{FF}} = 4 \cdot E_{\mathrm{CO_2,3mo}} \cdot \frac{2.14 \text{ ppm}}{\text{Gt C}} \cdot \overline{f} \quad [1]$$

where $E_{\mathrm{CO_2,3mo}}$ is the three month total CO_2 emissions and $\overline{f}$ is the average airborne fraction computed from all of the OCO-2 data; each three-monthly airborne fraction (f) is computed as:

$$f = \frac{R_{\mathrm{OCO-2,3mo}}}{E_{\mathrm{CO_2,3mo}} \cdot 2.14 \text{ ppm/Gt C}} \quad [2]$$

where $R_{\mathrm{OCO-2,3mo}}$ is the three-monthly growth rate computed from the OCO-2 data.

The TCCON CH_4 series shown in Fig. 6b are computed from the time series and trends in Fig. 6a. First, the percent difference of the northern and southern hemisphere data against their respective trends is computed. Then, monthly averages of these two percent differences are calculated. Finally, the two monthly time series are averaged together.

The box model trend shown in Fig. 6b was calculated using the box model described in (33) and (34), available at https://github.com/alexjturner/BoxModel_PNAS_20161223. Briefly, this model treats the change in concentration of CH_4 in each hemisphere as the sum of changes due to emissions, oxidation by OH, and interhemispheric transport. OH concentrations can either be directly prescribed or have a prescribed source with concentrations varying alongside CH_4 and CO. The results in Fig. 6b use prescribed OH concentrations, but the behavior is similar if the OH source is prescribed. For simplicity, CH_4 emissions followed the "stabilized" scenario described in (34). The percent difference in CH_4 shown in Fig. 6b is the difference between a model run with a 3% reduction in OH during 2020 and one without.

We do note that, in the box model, the renewed CH_4 growth after 2008 occurs earlier than indicated by in situ measurement. This is due to the timing of CH_4 emissions growth in the EDGAR inventory. However, this does not affect our conclusions as (a) we use the difference of two model runs with the same CH_4 emissions trends and (b) we focus on the behavior in 2020.

TROPOMI NO_2 timeseries. For our analysis we re-grid the operational TROPOMI tropospheric vertical column NO_2, with native pixels of approximately 3.5×7 km^2 for 2019 and 3.5×5.5 km^2 for 2020, to a newly defined $0.01^\circ \times 0.01^\circ$ grid (approximately 1×1 km^2) centered over each of the three cities: Los Angeles, Lima, and Shanghai. Before re-gridding, the data are filtered so as to use only the highest quality measurements (quality assurance flag (QA_flag) > 0.75). By restricting to this QA value, we are removing mostly cloudy scenes (cloud radiance fraction > 0.5) and observations over snow-ice. Once the re-gridding has been completed, the data is binned temporally during a 15-day rolling timeframe and spatially over the metropolitan area, which we loosely define as a $1^\circ \times 1^\circ$ box over the city center. The rolling 75th percentile of the binned data during the first five months of 2019 annd 2020 are shown in top row of Figure 7. There is some evidence that the current TROPOMI operational NO_2 product may have a low bias of 20 to 40% in polluted areas; much of this bias may be attributed to the air mass factor (35–37). We limit our analysis to relative trends, which reduces this uncertainty.

LA Basin AQ analysis. The hourly ambient temperature and concentrations of PM2.5, NO_2, and O_3 in the South Coast Air Basin for the period of 1 Jan 2015 to 30 Sept 2020 were downloaded from the California Air Resources Board Air Quality Data Query Tool (https://www.arb.ca.gov/aqmis2/aqdselect.php). It should be noted that the 2020 data are preliminary, unvalidated, and subject to change. The following steps were taken for data analysis:

1. Only the monitoring sites that had complete data between 2015 and 2020 were considered in this analysis. Near-road monitoring sites were not included in the analysis. Figure S11 and Table S3 show the location of the monitoring sites considered in this analysis and the parameters measured at each site, respectively.

2. For every date and site, the 1hr daily maximum (DM) temperature, 24hr average PM2.5, 1hr DM NO_2, and 8hr average DM O_3 were calculated.

3. For every date, the average of the above-mentioned parameters was calculated across all monitoring sites. 7-day moving averages were then calculated and presented by day of year in Figure 8 for 2020 and the average ($\pm$ range) of [2015-2019]. The background colors in Figure 8 illustrate the difference between the 7-day moving average temperature in 2020 and the average ($\pm 1\sigma$) temperature in [2015-2019] by day of year.

4. Using the data in step 2, the percent change in monthly average concentrations of 1hr DM NO_2 and 8hr DM O_3 between 2020 and the average of [2015-2019] was calculated by month and site as shown in Figures S1 and S2.

Global ozone production efficiency calculation. We evaluated the seasonal and regional changes in the global tropospheric ozone response to COVID-19 NO_x emissions using a state-of-the-art chemical data assimilation system. Anthropogenic NO_x emission reductions linked to the COVID-19 pandemic were estimated as the difference between 2020 emissions and climatological (baseline) emissions for 2010-2019 estimated from our decadal chemical reanalysis constrained by multiple satellite measurements. The assimilation system uses the MIROC-CHASER global chemical transport model and an ensemble Kalman filter technique (38). This approach allows us to capture temporal and spatial variations in transport and chemical

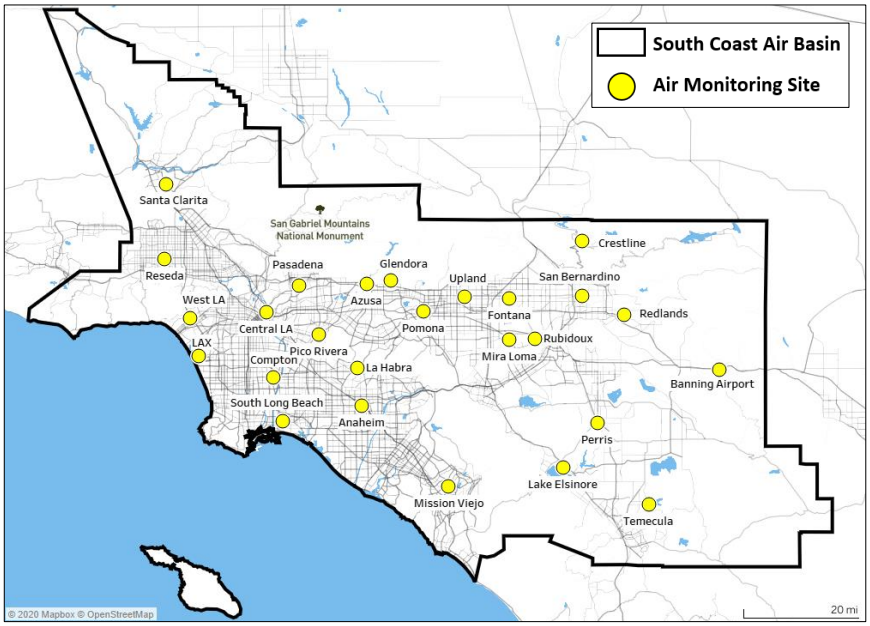

Fig. S11. Location of South Coast Air Basin monitoring sites included in this analysis.

Site	Temperature	O_3	PM2.5	NO_2
Anaheim	✓	✓	✓	✓
Azusa	✓	✓		✓
Banning airport	✓	✓	✓	✓
Central LA	✓	✓	✓	✓
Compton	✓	✓		✓
Crestline	✓	✓	✓	
Fontana	✓	✓		✓
Glendora	✓	✓	✓	✓
La Habra		✓		✓
Lake Elsinore	✓	✓	✓	✓
LAX		✓		✓
Mira Loma	✓	✓	✓	✓
Mission Viejo	✓	✓		
Pasadena		✓		✓
Perris	✓	✓		
Pico Rivera	✓	✓		✓
Pomona		✓		✓
Redlands		✓		
Reseda		✓	✓	✓
Rubidoux	✓	✓	✓	✓
San Bernadino	✓	✓		✓
Santa Clarita	✓	✓	✓	✓
South Long Beach			✓	
Upland	✓	✓	✓	✓
West LA		✓		✓
Temecula	✓	✓	✓	

Table S3. Parameters used from each South Coast Air Basin monitoring site.

reactions in the emission and concentration estimates. The results for 2020 were used previously to evaluate the air quality response to Chinese COVID-19 lockdown (39), and show reasonable agreements with the observed concentrations from in-situ, ozonesonde, and satellite ozone measurements globally for 2005-2018 (39) as well as for 2020 (40).

In order to evaluate seasonal and regional differences in the ozone response, the ozone production efficiency (OPE) was estimated based on model sensitivity calculations using the 2020 and baseline emissions for February-July 2020. The OPE was calculated using the simulated global tropospheric ozone burden changes corresponding to changing NO_x emissions (i.e., the COVID-19 emission anomaly); the analysis was performed separately for each of the selected megacities. The model simulations were conducted from the beginning to the end of each month for the time period February to June, 2020, using the same initial conditions. The simulated tropospheric ozone burden averaged over the last 5 days of each month was compared between the simulations using the 2020 and baseline emissions. The analysis thus provides information on monthly changes in the ozone response (Tg) to reduced NO_x emissions (Tg per year) for each megacity separately. These data are presented in Table S4.

PM2.5 simulations. We used the GEOS-Chem (v9-02) model with a bi-directional NH_3 flux scheme (41) at the nested resolution of $0.3125^\circ \times 0.25^\circ$ latitude to explore the sensitivity of inorganic aerosol formation to NO_x emission reductions in Los Angeles (118.239° W, 34.052° N) during COVID-19. Our detailed O_3-NO_x-VOC-aerosol simulations were driven by Goddard Earth Observing System (GEOS-FP 5.22.0) assimilated meteorological fields and include anthropgenic/biogenic/biomass burning emissions (42–44), gas-phase chemistry (45) and inorganic aerosol partitioning (46), wet/dry depositions (47–49) and transport. We first scaled anthropogenic NO_x and SO_2 emissions from HTAP v2 (42) (originally for the year 2010) to the year 2017 using satellite-derived SO_2 and NO_x emission reduction ratios (50) as our base emissions, which refer to emissions before lockdown during COVID-19. We scaled our base anthropogenic NO_x emissions in March by BAU/COVID monthly NO_x emission ratios from Miyazaki et al. (39) as our BAU/COVID emissions. In the COVID-19 simulations, the NO_x emissions started to decrease on March 1st.

We calculated the gas ratio (51) shown in Fig. S4 using Eq. (3):

$$\text{gas ratio} = \frac{[NH_3] + [NH_4^+] - 2[SO_4^{2-}]}{[HNO_3] + [NO_3^-]} \quad [3]$$

$[NH_3]$, $[NH_4^+]$, $[SO_4^{2-}]$, $[HNO_3]$ and $[NO_3^-]$ are in units of molar concentrations (mol m^{-3}) and include both gas-phase and aerosol-phase. This gas ratio is an indicator of NH_4NO_3 production sensitivity to NO_x emission change and NH_3 emission change. Values > 1 indicate that NH_4NO_3 production is NO_x limited; values < 1 indicate it is NH_3 limited.

Ozone production efficiency steady state model. The ozone production efficiency (OPE) values in Fig. S10 were computed from a HO_x-NO_x steady state model similar to that used in Laughner et al. (52) (available at https://github.com/joshua-laughner/HSSModel/releases/tag/v0.1.0, an example notebook is available at https://github.com/joshua-laughner/HOx-NOx-model-PNAS-2021). Briefly, this model takes fixed values for NO and NO_2 concentrations, VOC reactivity (VOC_R), HO_x productions ($P(HO_x)$), and RO_2 + NO branching ratio (α) and solves for RO_2, HO_2, and OH concentrations, assuming that HO_2, RO_2, and the whole HO_x family (RO_2 + HO_2 + OH) are in steady state.

Theoretical OPE is computed from the model steady state as the ratio of ozone production to NO_x loss, similar to Kleinman et al. (53) except that formation of alkyl nitrates is counted as NO_x loss:

$$\begin{aligned} \mathrm{OPE_{model}} &= \frac{P(\mathrm{O_3})}{L(\mathrm{NO_x})} \\ &= \frac{k_{\mathrm{NO+HO2}}[\mathrm{NO}][\mathrm{HO_2}] + (1-\alpha)k_{\mathrm{NO+RO2}}[\mathrm{NO}][\mathrm{RO_2}]}{k_{\mathrm{NO2+OH}}[\mathrm{NO_2}][\mathrm{OH}] + \alpha k_{\mathrm{NO+RO2}}[\mathrm{NO}][\mathrm{RO_2}]} \end{aligned} \quad [4]$$

	Country	City	Feb 2020	Mar 2020	Apr 2020	May 2020	Jun 2020
Δ total O_3 (Tg O_3)	China	Shanghai	-0.0159	-0.054	-0.0196	-0.079	-0.1659
	Pakistan	Karachi	-0.0009	-0.0023	-0.0039	0.0031	-0.0069
	India	Mumbai	-0.0075	-0.0067	-0.0077	-0.0053	-0.0538
	China	Beijing	-0.0064	-0.0087	0.0049	0.0033	-0.0227
	Turkey	Istanbul	-0.0032	-0.0136	-0.0041	-0.0151	-0.0353
	China	Guangzhou	-0.0127	-0.02	-0.0164	-0.0281	-0.0277
	India	Delhi	0.0014	0.0096	-0.0268	-0.0152	-0.0313
	Nigeria	Lagos	-0.0186	-0.0336	-0.0532	-0.0912	-0.0594
	South Korea	Seoul	-0.0155	-0.0246	-0.0386	-0.0476	-0.0553
	Brazil	São Paulo	-0.0226	-0.034	-0.0499	-0.039	-0.0308
	Indonesia	Jakarta	0.0043	-0.1095	-0.1149	-0.1084	-0.0961
	Mexico	Mexico City	-0.0221	-0.0376	-0.0817	-0.1191	-0.0879
	Japan	Tokyo	-0.0131	-0.014	-0.0107	-0.0116	-0.019
	United States	New York City	-0.0072	-0.0082	-0.0187	-0.0129	-0.014
	Egypt	Cairo	0.003	-0.0018	-0.0089	-0.0149	-0.0184
	Peru	Lima	-0.0095	-0.0396	-0.0686	-0.0518	-0.0558
	United Kingdom	London	-0.0076	-0.0104	-0.0113	-0.0102	-0.0149
	Iran	Tehran	-0.0141	-0.0105	-0.0442	-0.051	-0.0503
	Australia	Sydney	-0.3071	-0.3481	-0.3528	-0.3601	-0.2905
	United States	Los Angeles	-0.01	-0.02	-0.01	-0.07	-0.11
Δ NO_x emissions (Tg N)	China	Shanghai	-0.553854	-0.646131	-0.245612	-0.359558	-0.396624
	Pakistan	Karachi	0.00108	-0.01083	-0.013907	-0.010837	-0.020179
	India	Mumbai	-0.024593	-0.027663	-0.024419	-0.061499	-0.139134
	China	Beijing	-0.198961	-0.099599	-0.009603	-0.011923	-0.145126
	Turkey	Istanbul	-0.130658	-0.174579	-0.03314	-0.088187	-0.089888
	China	Guangzhou	-0.078471	-0.132469	-0.067583	-0.066167	-0.113306
	India	Delhi	0.013419	0.018727	-0.039327	-0.03435	-0.032617
	Nigeria	Lagos	-0.009639	-0.007365	-0.007956	-0.013574	-0.005402
	South Korea	Seoul	-0.149712	-0.159186	-0.203807	-0.148556	-0.29208
	Brazil	São Paulo	-0.008472	-0.027171	-0.0432	-0.039373	-0.033903
	Indonesia	Jakarta	0.002877	-0.047226	-0.064194	-0.026963	-0.05354
	Mexico	Mexico City	-0.01537	-0.06882	-0.061191	-0.137199	-0.054954
	Japan	Tokyo	-0.041926	-0.034649	-0.029087	-0.039731	-0.059888
	United States	New York City	-0.044813	-0.052346	-0.070999	-0.061666	-0.091085
	Egypt	Cairo	0.024929	-0.012549	-0.023062	-0.04617	-0.050889
	Peru	Lima	-0.002643	-0.01057	-0.015109	-0.017799	-0.020392
	United Kingdom	London	-0.056416	-0.086728	-0.136076	-0.114414	-0.143172
	Iran	Tehran	-0.108269	-0.081617	-0.12622	-0.145247	-0.140058
	Australia	Sydney	-0.122616	-0.090462	-0.125676	-0.177362	-0.151404
	United States	Los Angeles	-0.61	-0.53	-0.19	-0.31	-0.43
OPE (Tg O_3 / Tg N)	China	Shanghai	0.028708	0.083574	0.079801	0.219714	0.41828
	Pakistan	Karachi	-0.833333	0.212373	0.280434	-0.286057	0.34194
	India	Mumbai	0.304965	0.242201	0.315328	0.08618	0.386678
	China	Beijing	0.032167	0.08735	-0.510257	-0.276776	0.156416
	Turkey	Istanbul	0.024491	0.077902	0.123718	0.171227	0.392711
	China	Guangzhou	0.161843	0.150979	0.242665	0.424683	0.244471
	India	Delhi	0.10433	0.512629	0.681466	0.442504	0.959622
	Nigeria	Lagos	1.929661	4.562118	6.686777	6.718727	10.995927
	South Korea	Seoul	0.103532	0.154536	0.189395	0.320418	0.189332
	Brazil	São Paulo	2.667611	1.251334	1.155093	0.990527	0.908474
	Indonesia	Jakarta	1.494612	2.318638	1.789887	4.020324	1.79492
	Mexico	Mexico City	1.437866	0.546353	1.335164	0.868082	1.59952
	Japan	Tokyo	0.312455	0.404052	0.367862	0.291963	0.317259
	United States	New York City	0.160668	0.15665	0.263384	0.209191	0.153703
	Egypt	Cairo	0.120342	0.143438	0.385916	0.32272	0.361571
	Peru	Lima	3.5944	3.746452	4.54034	2.910276	2.736367
	United Kingdom	London	0.134714	0.119915	0.083042	0.08915	0.104071
	Iran	Tehran	0.130231	0.12865	0.350182	0.351126	0.359137
	Australia	Sydney	2.504567	3.848025	2.807219	2.030311	1.918708
	United States	Los Angeles	0.016393	0.037736	0.052632	0.225806	0.255814

Table S4. Changes in NO_x emissions, O_3, and ozone production efficiency inferred from the multi-satellite data assimilation system.

References

1. Liu J, Wennberg PO, Parazoo NC, Yin Y, Frankenberg C (2020) Observational constraints on the response of high-latitude northern forests to warming. *AGU Advances* 1(4).
2. Graven HD, et al. (2013) Enhanced seasonal exchange of CO2 by northern ecosystems since 1960. *Science* 341(6150):1085–1089.
3. Fyfe JC, et al. (2021) Quantifying the influence of short-term emission reductions on climate. *Science Advances* 7(10).
4. Hale T, et al. (2020) Oxford COVID-19 government response tracker. Blavatnik School of Government.
5. Strohmeier M, Olive X, Lübbe J, Schäfer M, Lenders V (2020) Crowdsourced air traffic data from the OpenSky network 2019–20. *Earth System Science Data Discussions* 2020:1–15.
6. Boersma KF, et al. (2017) QA4ECV NO_2 tropospheric and stratospheric column data from OMI. doi: 10.21944/QA4ECV-NO2-OMI-V1.1.
7. Boersma KF, et al. (2018) Improving algorithms and uncertainty estimates for satellite NO_2 retrievals: results from the quality assurance for the essential climate variables (QA4ECV) project. *Atmospheric Measurement Techniques* 11(12):6651–6678.
8. van Geffen J, et al. (2020) S5P TROPOMI NO_2 slant column retrieval: method, stability, uncertainties and comparisons with OMI. *Atmospheric Measurement Techniques* 13(3):1315–1335.
9. Deeter MN, et al. (2017) A climate-scale satellite record for carbon monoxide: the MOPITT Version 7 product. *Atmospheric Measurement Techniques* 10(7):2533–2555.
10. Krotkov NA, et al. (2016) Aura OMI observations of regional SO_2 pollution changes from 2005 to 2015. *Atmospheric Chemistry and Physics* 16(7):4605–4629.
11. Can Li, Nickolay A. Krotkov PL, Joiner J (2020) OMI/Aura Sulphur Dioxide (SO_2) Total Column 1-orbit L2 Swath 13x24 km V003, Greenbelt, MD, USA, Goddard Earth Sciences Data and Information Services Center (GES DISC). Accessed: 11 Nov 2020, doi: 10.5067/Aura/OMI/DATA2022.
12. Livesey NJ, et al. (2018) Earth Observing System (EOS) Aura Microwave Limb Sounder (MLS) Version 4.2x Level 2 and 3 data quality and description document (JPL D-33509 Rev. E). Available from, https://mls.jpl.nasa.gov/data/v4-2_data_quality_document.pdf, last access: 21 Nov 2020.
13. Schwartz M, Froidevaux L, Livesey N, Read W (2015) MLS/Aura Level 2 Ozone (O_3) Mixing Ratio V004, Greenbelt, MD, USA, Goddard Earth Sciences Data and Information Services Center (GES DISC). doi: 10.5067/Aura/MLS/DATA2017.
14. Manney G, Santee M, Froidevaux L, Livesey N, Read W (2015) MLS/Aura Level 2 Nitric Acid (HNO_3) Mixing Ratio V004, Greenbelt, MD, USA, Goddard Earth Sciences Data and Information Services Center (GES DISC). doi: 10.5067/Aura/MLS/DATA2012.
15. Science Data Operations System Jet Propulsion Laboratory (2019) Oco-2 level 2 geolocated XCO2 retrievals results, physical model, retrospective processing v10r.
16. O'Dell CW, et al. (2018) Improved retrievals of carbon dioxide from Orbiting Carbon Observatory-2 with the version 8 ACOS algorithm. *Atmospheric Measurement Techniques* 11(12):6539–6576.
17. Kiel M, et al. (2019) How bias correction goes wrong: measurement of x&ltsub&gtCO&ltsub&gt2&lt/sub&gt&lt/sub&gt affected by erroneous surface pressure estimates. *Atmospheric Measurement Techniques* 12(4):2241–2259.
18. Wunch D, et al. (2015) The Total Carbon Column Observing Network's GGG2014 data version, Technical report.
19. Wennberg PO, et al. (2014) TCCON data from Park Falls (US), Release GGG2014R0 (TCCON data archive, hosted by CaltechDATA).
20. Sherlock V, et al. (2014) TCCON data from Lauder (NZ), 125HR, Release GGG2014R0 (TCCON data archive, hosted by CaltechDATA).
21. Pollard DF, Robinson J, Shiona H (2019) TCCON data from Lauder (NZ), Release GGG2014.R0 (TCCON data archive, hosted by CaltechDATA).
22. Oda T, Maksyutov S, Andres RJ (2018) The open-source data inventory for anthropogenic CO_2, version 2016 (ODIAC2016): a global monthly fossil fuel CO_2 gridded emissions data product for tracer transport simulations and surface flux inversions. *Earth System Science Data* 10(1):87–107.
23. Liu Z, et al. (2021) Global daily CO_2 emissions for the year 2020.
24. Schäfer M, Strohmeier M, Lenders V, Martinovic I, Wilhelm M (2014) Bringing Up OpenSky: A Large-scale ADS-B Sensor Network for Research. *Proceedings of the 13th IEEE/ACM International Symposium on Information Processing in Sensor Networks (IPSN)* pp. 83–94.
25. Olive X (2019) traffic, a toolbox for processing and analysing air traffic data. *Journal of Open Source Software* 4(39).
26. Laughner J (2020) COVID Atmospheric Ancillary Data Agglomerator, v0.1.0.
27. Hale T, et al. (2021) A global panel database of pandemic policies (Oxford COVID-19 government response tracker). *Nature Human Behaviour* 5(4):529–538.
28. Friedlingstein P, et al. (2019) Global carbon budget 2019. *Earth System Science Data* 11(4):1783–1838.
29. Le Quéré C, et al. (2020) Temporary reduction in daily global CO_2 emissions during the COVID-19 forced confinement. *Nature Climate Change* 10(7):647–653.
30. Liu Z, et al. (2020) Near-real-time monitoring of global CO_2 emissions reveals the effects of the COVID-19 pandemic. *Nature Communications* 11(1).
31. Saunois M, et al. (2020) The global methane budget 2000–2017. *Earth System Science Data* 12(3):1561–1623.

32. IEA (2021) Methane tracker 2021 (https://www.iea.org/reports/methane-tracker-2021). last accessed 22 Apr 2021.
33. Turner AJ, Frankenberg C, Wennberg PO, Jacob DJ (2017) Ambiguity in the causes for decadal trends in atmospheric methane and hydroxyl. *Proceedings of the National Academy of Sciences* 114(21):5367–5372.
34. Turner AJ, Frankenberg C, Kort EA (2019) Interpreting contemporary trends in atmospheric methane. *Proceedings of the National Academy of Sciences* 116(8):2805–2813.
35. Griffin D, et al. (2019) High-resolution mapping of nitrogen dioxide with TROPOMI: First results and validation over the Canadian oil sands. *Geophysical Research Letters* 46(2):1049–1060.
36. Judd LM, et al. (2020) Evaluating Sentinel-5P TROPOMI tropospheric NO_2 column densities with airborne and Pandora spectrometers near New York City and Long Island Sound. *Atmospheric Measurement Techniques* 13(11):6113–6140.
37. Verhoelst T, et al. (2020) Ground-based validation of the copernicus Sentinel-5p TROPOMI NO_2 measurements with the NDACC ZSL-DOAS, MAX-DOAS and Pandonia global networks. *Atmospheric Measurement Techniques Discussions* 2020:1–40.
38. Miyazaki K, et al. (2020) Updated tropospheric chemistry reanalysis and emission estimates, TCR-2, for 2005–2018. *Earth System Science Data* 12(3):2223–2259.
39. Miyazaki K, et al. (2020) Air quality response in China linked to the 2019 novel coronavirus (COVID-19) lockdown. *Geophysical Research Letters* 47(19):e2020GL089252. doi: 10.1029/2020GL089252.
40. Miyazaki K, et al. (2021) Global tropospheric ozone responses to reduced NO_x emissions linked to the COVID-19 world-wide lockdowns. *Science Advances* 7(24):eabf7460.
41. Zhu L, et al. (2015) Global evaluation of ammonia bidirectional exchange and livestock diurnal variation schemes. *Atmospheric Chemistry and Physics* 15(22):12823–12843.
42. Janssens-Maenhout G, et al. (2015) HTAP_v2.2: a mosaic of regional and global emission grid maps for 2008 and 2010 to study hemispheric transport of air pollution. *Atmospheric Chemistry and Physics* 15(19):11411–11432.
43. Guenther AB, et al. (2012) The model of emissions of gases and aerosols from nature version 2.1 (MEGAN2.1): an extended and updated framework for modeling biogenic emissions. *Geoscientific Model Development* 5(6):1471–1492.
44. van der Werf GR, et al. (2010) Global fire emissions and the contribution of deforestation, savanna, forest, agricultural, and peat fires (1997–2009). *Atmospheric Chemistry and Physics* 10(23):11707–11735.
45. Mao J, et al. (2010) Chemistry of hydrogen oxide radicals (HO_x) in the arctic troposphere in spring. *Atmospheric Chemistry and Physics* 10(13):5823–5838.
46. Park RJ (2004) Natural and transboundary pollution influences on sulfate-nitrate-ammonium aerosols in the United States: Implications for policy. *Journal of Geophysical Research* 109(D15).
47. Liu H, Jacob DJ, Bey I, Yantosca RM (2001) Constraints from ^{210}Pb and ^{7}Be on wet deposition and transport in a global three-dimensional chemical tracer model driven by assimilated meteorological fields. *Journal of Geophysical Research: Atmospheres* 106(D11):12109–12128.
48. Wang Q, et al. (2011) Sources of carbonaceous aerosols and deposited black carbon in the arctic in winter-spring: implications for radiative forcing. *Atmospheric Chemistry and Physics* 11(23):12453–12473.
49. Amos HM, et al. (2012) Gas-particle partitioning of atmospheric Hg(II) and its effect on global mercury deposition. *Atmospheric Chemistry and Physics* 12(1):591–603.
50. Miyazaki K, et al. (2019) Chemical reanalysis products, doi: 10.25966/9qgv-fe81.
51. Ansari AS, Pandis SN (1998) Response of inorganic PM to precursor concentrations. *Environmental Science & Technology* 32(18):2706–2714.
52. Laughner JL, Cohen RC (2019) Direct observation of changing NO_x lifetime in North American cities. *Science* 366(6466):723–727.
53. Kleinman LI, et al. (2002) Ozone production efficiency in an urban area. *Journal of Geophysical Research: Atmospheres* 107(D23):ACH 23–1–ACH 23–12.